Long-range angular correlations in soft and hard pPb collisions at a center-of-mass energy of $5.02\,\mathrm{TeV}$ measured with ALICE

Master Thesis
by
Christian Bourjau

LUND
UNIVERSITY

March 21, 2014

Supervisor:
Peter Christiansen

Department of Physics
Lund University

Abstract

Previous studies of two-particle correlation in proton-lead (pPb) collisions at $\sqrt{s} = 5.02\,\text{TeV}$ revealed a so-called *double ridge* structure similar to the one observed in lead-lead (PbPb) collisions. This structure features two distinct ridges extending over the entire $\Delta\eta$ range (long-range correlations) at $\Delta\varphi \approx 0$ (near-side) and $\Delta\varphi \approx \pi$ (away-side). A model based on hydrodynamical expansion is capable of modeling this effect but requires that a spatially extended strongly-interacting medium is created. While such an assumption is reasonable for PbPb collisions, it is not justifiable in pPb collisions creating the need of an alternative description of the effect in the latter system. The following thesis presents the aforementioned hydrodynamical model and two proposed alternatives: The Color Glass Condensate and Color Reconnection (CR). A falsification of the models is undertaken by studying the dependence of the two-particle correlations on the *hardness* of the underlying events. A multiplicity dependent bias towards di-jets in low multiplicity events was introduced by hardening the event sample, leaving the long-range near-side area of the double ridge for the extraction of an unbiased *ridge yield*. No dependence of the ridge yield on the hardness of the event was found within the margin of uncertainty. This observation disfavors CR but detailed theoretical studies of CR in pPb and the study of a so-called *soft* event sample are needed to rule out this model conclusively.

Populärvetenskaplig sammanfattning

Den rådande och även allmänt kända teorin för Universums uppkomst kallas *Big Bang*-teorin. Big Bang tros ha inträffat för cirka 13,8 miljarder år sedan och beskriver en tid när vårt Universum befann sig i ett mycket varmt och energitätt tillstånd, som snabbt kyldes ner för att bilda de första lätta atomkärnorna bara några minuter in i sitt unga liv. Även om det tog ytterligare 100 miljoner år för de första stjärnorna att bildas från orörda moln av helium och deuterium tror man att många av de mest intressanta och olösta frågorna i fysiken manifesterade sig i den allra första mikrosekunden: Varför finns det så lite antimateria? Var kommer den mystiska mörka materien ifrån vilken gör att galaxer roterar snabbare än de borde? Var de fyra krafterna som vi känner idag (gravitation, elektromagnetism, stark kraft och svag kraft) en gång i tiden förenade till en?
Om mänskligheten strävar efter att förstå vilken typ av värld vi lever i är det oundvikligt att studera denna mycket viktiga första mikrosekund. Vid denna tidpunkt var temperaturen och partikeldensiteten så hög att inga kärnor ännu bildats. Istället var all materia i ett tillstånd som kallas kvark-gluon-plasma (quark gluon plasma, QGP) där de grundläggande kvarkarna och gluonerna kunde existera som fria partiklar och inte begränsades till hadroner (uppsättningar av två eller tre kvarkar) som de är nästan överallt idag. Ett sådant QGP kan återskapas och studeras genom att kollidera tunga atomkärnor (t.ex. bly) med den mest kraftfulla kolliderare som finns idag: the Large Hadron Collider (LHC). Plasmat kommer endast att existera för ett mycket kort ögonblick innan det kyls ner så mycket att det upplöses i hadroner. Innan det händer genomgår plasmat en dynamisk utveckling som påminner om en utsträckt vätskedroppe. En kvarleva av denna utveckling kan ses genom att noggrant studera de hadroner som skapas under nedkylningen. Det observerades att de producerade hadronernas densitet och genomsnittliga rörelsemängd förstärktes inom ett givet plan och undertrycktes vinkelrät mot detta.
Denna effekt förväntades i bly-bly kollisioner eftersom två stora kärnor antogs skapa ett jämförelsevis stort plasma. Å andra sidan förväntades proton-bly kollisioner bara skapa mycket små plasmavolymer som borde ge litet eller inget kollektivt beteende. Ändå uppvisade proton-bly kollisioner en liknande effekt som den i bly-bly kollisioner när de först analyserades i december 2012. Sedan dess har stora ansträngningar gjorts för att förstå denna effekt och flera konkurrerande teorier har framkommit som måste verifieras eller falsifieras av experimentalfysiker.
Denna avhandling presenterar och studerar tre av dessa teorier och deras förväntade respons om man använder dem på en viss typ av kollision som kallas en *hård* process. Sådana processer isolerades även i tillgängliga mätdata och jämfördes med teoretiska förutsägelser.
Analysen som presenteras här är baserad på två-partikel-korrelationer, vilket innebär att vinkelavstånden mellan uppsättningar av två partikelspår utvärderas. Om ett stort antal kollisioner analyseras framträder ett mönster som visar den ovan beskrivna förhöjningen inom ett plan.

Acknowledgements

I would like to send out my thanks and appreciation to everyone how supported me, directly or indirectly, in the making of this theses. The first of may of these people is my supervisor Peter Christiansen who not only proposed this analysis but also provided me with fresh ideas and solutions from start to end. The help and excellent discussions I had with Evert Stenlund and Anders Oskarsson were also indispensable and always much appreciated. I also want to extend my thanks to my colleagues Carsten Søgaard, Tuva Richert, Martin Ljunggren and Vytautas Vislavičius for the many work and non-work related discussions and I hope to not have permanently divided our group with the very first sentence of the later introduction.
Since this list is, of cause, not the least bit exhaustive I also want to specifically thank everyone how could not be named here. Without all of you it would have been neither possible to conclude this thesis nor to have such a splendid time doing so. Thank you very much!

Contents

List of Figures

Chapter 1

Introduction

Elementary particle physics is the study of everything. While this statement might seem rather shallow and fishing for attention (which it is), it is still true in many more ways than one would initially think. Elementary particle physics studies the fundamental building blocks of all the types of matter ever observed. It is valid here in Lund, Sweden just as well as at the most distant outskirts of the universe - and it is believed to always have been and always will continue to do so. Even split seconds after the Big Bang the laws of particle physics governed the properties of this extremely hot and dense soup of matter evolving into the vast variety of particles known today.
However, many of the fundamental laws are not yet understood or even discovered, despite decades of work by thousands of physicists. During this time, larger and larger particle accelerators were built reproducing the state of matter at ever decreasing time scales after the Big Bang.
The current record holder in this quest is CERN with its *Large Hadron Collider* (LHC), being able to collide particles at unprecedented energies and frequencies. The LHC houses four experiments each having a specific scope. The one focused on studying matter at extreme conditions such as the Big Bang, which is created when colliding lead nuclei (PbPb), is the ALICE experiment. When the first results of such collisions became available in 2011 they appeared to be in agreement with previous studies predicting that PbPb collisions at the LHC will be able to create a state of matter known as the *Quark Gluon Plasma* (QGP). Intriguingly, conducting studies on proton-lead (pPb) collisions yielded similar results, though the creation of the QGP was deemed impossible in this collision system. Since then, several new or refined models were proposed to explain these experimental observations. Thus, the ball is back in the experimentalist's court to gather evidence for which theories hold, which need to be refined and which should be discarded.
This thesis presents the methods and findings from investigating so called *hard* pPb collisions by means of two-particle angular correlations. Subsequently, the yielded results are compared to the anticipated results of three possible models explaining the state of matter created at pPb collisions. The goal of this thesis was to provide new insights into the structure of proton-nucleus collisions and thus contributing to ultimately ruling out some, or confirming other models.
The work conducted during this project included a complete implementation[1] of the two-particle correlations method described in chapter 4. Furthermore, considerable time and effort was spend on further studies regarding the autocorrelations introduced by detector deficiencies, particle den-

[1] The complete source code excluding non-public data files may be found at [10]

sities and detector acceptances. These studies led to a novel, less model dependent and less complex efficiency correction method for two-particle correlation studies.
The following chapter introduces the main concepts of the Standard Model before summarizing important results of heavy ion physics. A focus is then placed on the observation of the so-called *flow-like* phenomena in pPb collisions. Three models that can possibly explain this effect are introduced and their anticipated responses to a hardened event sample are discussed. Chapter 3 describes the LHC and the ALICE experiment as well as the detectors of interest to the carried out analysis. The fourth chapter first covers the event and track selection criteria before describing the extraction and correction of two-particle correlation from the event sample. Subsequently, the *subtraction* method revealing the flow like phenomenon is discussed and the applied methods are tested for Monte Carlo closure. Results are presented in chapter 5 while their discussion takes place in chapter 6. Finally, a summary and outlook is given in the last chapter.

Chapter 2

Introduction to Heavy Ion Physics

2.1 The Standard Model

The Standard Model (SM) is the current theoretical framework used to describe all microscopic processes. It contains all the known fundamental particles and describes the interactions among them via the strong, weak, and electromagnetic force. While the current formulations stems from the late 1970s, many of its concepts date back further and were developed by a joint effort of many physicists. All particles in this theory are believed to be point like, i.e. are fundamental. Albeit being extraordinarily successful at explaining most experimental results and predicting novel phenomena, the SM is known to be an incomplete theory since it does neither contain a dark matter candidate nor a quantum description of gravity. An example of its success are studies of the electron magnetic moment $g/2$: The SM prediction agree with current experimental over more than ten orders of magnitude [30]. The latest and possibly most public achievement was the discovery of the Higgs boson in 2013, which was introduced to the SM to assign masses to its particles.

All dynamics and kinematics of the SM are governed by the Lagrangian $\mathcal{L}$ which may be split up into three sectors as $\mathcal{L} = \mathcal{L}_{EW} + \mathcal{L}_{QCD} + \mathcal{L}_{H}$. The following sections will explain the fields (yielding leptons, quarks and the Higgs boson) as well as the interactions (gauge bosons) between them in more detail.

2.1.1 Leptons and quarks

All matter particles and force carriers of the standard model are depicted in fig. 2.1. The former are separated into leptons (green) and quarks (purple). Each is again composed of three families (often also called generations or flavors) depicted by columns in the figure. All quarks and all leptons are spin $1/2$ particles and thus fermions; however, they differ in various other properties. Each lepton family consists of one massive particle with an electric charge $-1e$ (e being the electron charge) and one neutral, very light, particle called a neutrino. The charged particles are the electron e, muon μ or tau τ. Additionally to the electric charge, leptons carry an electron number (L_e), a muon number (L_μ) and a tau number (L_τ) which is either 1 if the particle is a

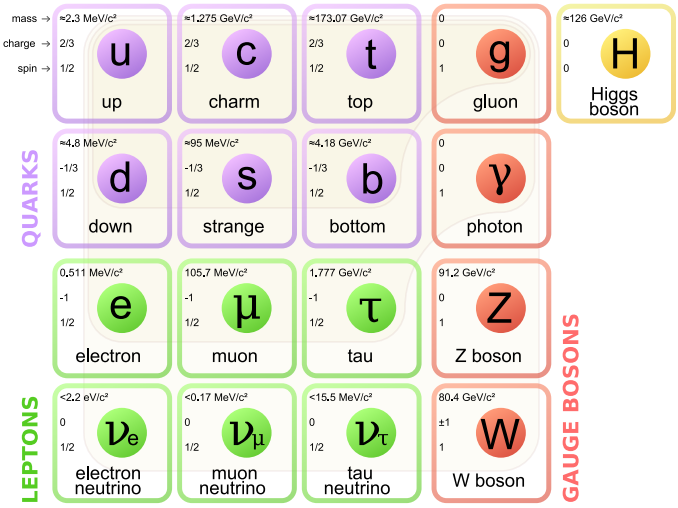

Figure 2.1: Summary of all the fundamental particle of the Standard model. The three families of the quarks and leptons are given by their respective column. The shaded backgrounds indicate to which fermions each gauge boson couples. From [16].

member of the respective family or 0 otherwise.

The six quarks, up (u), down (d), strange (s), charm (c), bottom (b) and top (t) have masses rising in this order. u, c and t have electrical charge $2/3e$ while d, s and b are charged by $-1/3e$. A property unique to quarks is the so called color charge: each quark carries either a red, green or blue color. The implications of this quantum number is further discussed after the introduction of the force carriers in sec. 2.1.2.
For each lepton exists a corresponding anti-particle with the exact same mass but all the quantum numbers inverted. In case of color, the inverse is defined as “anti-red”, “anti-green” and “anti-blue”.

2.1.2 The gauge bosons

From a mathematical point of view, all the particles of the SM are described as fields and all the interaction arise from a local $SU(3) \times SU(2) \times U(1)$ symmetry of $\mathcal{L}$. In a simplified picture, this means that $\mathcal{L}$ remains unchanged if all the fields are transformed by any set of matrices from the $SU(3) \times SU(2) \times U(1)$ group. $SU(3)$ acts on the three dimensional color space, $SU(2)$ on the two dimensional spin space and $U(1)$ on the electric charge. Interactions are mediated by so called gauge bosons - particles of spin 1.

The electroweak sector

The $\mathcal{L}_{EW}$ sector of the Lagrangian exhibits a $SU(2) \times U(1)$ symmetry. This gives rise to the electromagnetic force (described by the theory of Quantum Electrodynamics (QED)) and the weak force. The two were unified to the so called electroweak force. All the transformations of the

$SU(2)$ group may be achieved with three two dimensional matrices - the Pauli matrices. They are called the generators of the group and give rise to the 3 interaction fields W^+, W^- and W^0. The $U(1)$ group has one such generator yielding the B^0 field. The theory of electroweak unification requires a mixing between the W^0 and B^0 fields and thus the four observable gauge bosons mediating the electroweak force are: The photon γ, the uncharged Z boson and the two oppositely charged $W^\pm$ bosons. Even though these four particles have such a similar origin they behave very differently. The γ, the mediator of the electromagnetic force, is doubtlessly the most prominent of these four bosons in every day life. This stems from it being massless and thus having a infinite range; hence, one can observe light even from the most distant objects in the universe. The photon couples to every particle with an electric charge, therefore to all quarks, e, μ, τ and also to the $W^\pm$ but notably not to itself.
The weak force is mediated by the remaining Z and $W^\pm$ which have many differences as compared to γ. Firstly, they are massive[1]; the Z weighs $90.2\,\mathrm{GeV/c^2}$ and the $W^\pm$ $80.4\,\mathrm{GeV/c^2}$. This limits the range of this force substantially, since the time interval between emission and absorption must be sufficiently small to not violate energy conservation. This time span Δt is given by the energy-time uncertainty

$$mc^2\Delta t < \frac{\hbar}{2} \tag{2.1}$$

where m is the mass of the gauge boson in question, c the speed of light in vacuum and $\hbar$ the reduced Planck constant. Thus, even if assuming that the created boson were to travel at the speed of light it may not reach farther than

$$R_F \approx c\Delta t \approx \frac{\hbar}{2mc^2} \tag{2.2}$$

which yields $\sim 10^{-3}$fm in case of the weak force.

The quantum chromodynamics sector

When investigating the Quantum Chromodynamics (QCD) sector of the Lagrangian ($\mathcal{L}_{QCD}$) many of the above introduced concepts can be applied again. $\mathcal{L}_{QCD}$ has a $SU(3)$ symmetry; any transformation in this group can be written in the form of eight complex 3×3 matrices called the Gell-Mann matrices. Again, each of these generators gives rise to a gauge boson. In the case of QCD they are called gluons, are massless, and carry exactly one color and one anti-color charge. They only couple to other color-charged particles, namely all quarks but also to them self.
The masslessness might suggest that the gluon has an infinite range just like the photon, this, however, is not the case. The self-coupling of the gluons leads to the fundamentally important effect of *confinement* and *asymptotic freedom*. If a color polarization of the vacuum would only stem from quark anti-quark pairs, a decrease in apparent color charge would be observed for lower energy interactions, analogous to the screening of electric charges in QED. In case of QCD, however, the fluctuations also include gluons. This leads to the effect that color charges appear augmented at increasing distance. Hence, quarks will feel a stronger attraction towards one another the further they are apart, effectively confining them inside so-called *hadrons*. This also prohibits

[1] Technically, they are massless in the theory of electroweak unification but acquire masses via the Higgs mechanism (cf. sec. 2.1.2)

the observation of isolated quarks. On the other hand, the strong force is attenuated for two quarks in close proximity, which is aptly referred to as *asymptotic freedom*.
Hadrons are color singlets and are classified as *mesons* and *baryons*. Mesons consist of one quark and one antiquark of opposite color charge. Baryons are composed of either three matter or antimatter quarks, whereas each of the three colors is present. Other color singlets such as a four quarks tetraquark or a glueball composed only of gluons were not yet observed with sufficient statistical certainty [6, 15].
During particle collisions a constituent of a hadron might receive a large momentum transfer driving it away from the remaining hadron. This causes the creation of a color field of high energy density which will eventually "break" by creating a quark-antiquark pair of opposite color charge, causing the creation of two separate hadrons. Depending on the magnitude of the initially transferred energy this process might repeat itself several times causing a cone shaped spray of particles known as a *jet*.

The Higgs sector

For the complete SM model Lagrangian to be invariant under the $SU(3)\times SU(2)\times U(1)$ symmetry it is necessary for all gauge bosons to be initially massless. This is solved by letting the particles acquire mass via an interaction with at least one additional field. Such interactions are combined in the Higgs sector $\mathcal{L}_H$ and just as in the above, a field excitation may be interpreted as a particle. While the Higgs mechanism was first theorized already in 1964 by François Englert, Robert Brout [20] and Peter Higgs [26] it was first confirmed experimentaly with the discovery of the Higgs particle in 2013.

2.1.3 Probing the Standard Model

In the above, the three parts of the Lagrangian, $\mathcal{L} = \mathcal{L}_{EW} + \mathcal{L}_{QCD} + \mathcal{L}_H$ were discussed from a theoretical point of view. Having the mathematical tools at hand does not, however, guarantee that it is readily possible to state falsifiable predictions. The Higgs boson was theorized more than 40 years ago but the accelerator technologies were not capable of producing it in a statistically significant amount until the Large Hadron Collider (LHC).
The QED sector, on the other hand, proofed to be easier to tame, which becomes apparent in the repeatedly extraordinarily precise comparison of its theory to experiments. The most prominent example being the $g/2$ factor mentioned in the beginning of this chapter. This kind of thorough testing is made possible since higher order interaction are strongly suppressed and may thus be disregarded without much loss in precision. Such an approach is referred to as perturbation theory and is applicable if the coupling strength of the underlying interaction is small; which is the case in all accessible energies for the QED sector.
The theory of QCD also had its early successes with the confirmation of quarks as elementary particles. At the same time, confinement explained why no quarks could be observed isolated. This phenomenon, however, also manifests itself in the *running coupling* strength α_S, which yields a new problem: Interactions with a small momentum transfer ($< 2\,\text{GeV/c}$) exhibit a coupling strength of order 1, which makes a perturbative treatment like in QED impossible. Strong interactions with a low momentum transfer are therefore notoriously challenging to understand. On

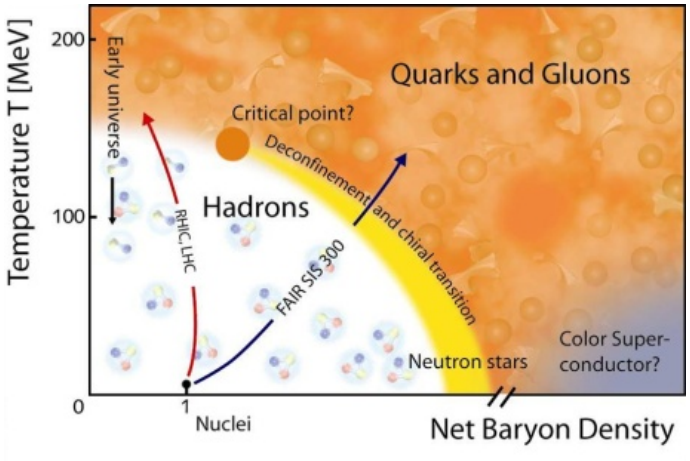

Figure 2.2: QCD phase diagram. From [33].

the other hand, this does neither imply that all interactions with a high momentum transfer are easy to calculate. Both momentum regions require individual models and approximations and are thus often referred to as *soft* and *hard*. While this nomination is not strictly defined, the separation is usually made at a momentum transfer of $\sim 2\,\mathrm{GeV/c}$. These computational difficulties are enhanced even more if the collisions involve heavy ions such as lead (Pb).
What is then the reason for choosing proton-nucleus (pA) or nucleus-nucleus (AA) as colliding systems? Contrary to pp collisions, heavy ion collisions allow the creation of a very hot and dense matter where the quarks are deconfined within this "macroscopic" volume. Studying the properties of QCD under these extreme conditions will help to falsify or confirm several theories that are supposed to apply to these "free" quarks and gluons. The most important findings and concepts from these studies are summarized below.

2.2 Highlights from the study of heavy ion collisions

2.2.1 Quark gluon plasma

Analogous to thermodynamical models one can picture a phase diagram of matter depicting the state of matter at a given baryonic density [2] and temperature. Such a diagram is shown in fig. 2.2. The low temperatures and densities we experience today are clearly in the hadronic phase, ie. quarks are confined in mesons and baryons. In the very early stages of the universe, however, the temperature is assumed to have been sufficiently high to prevent hadronization of matter. This state of matter is referred to as Quark Gluon Plasma (QGP) and is composed of deconfined quarks and gluons. Numerical QCD calculations suggest that this state of matter is produced in heavy ion collisions at the LHC. However, the created QGP will follow a fast dynamic evolution towards hadronization. Thus the QGP evades direct probing and its properties may only be inferred by the hadronic particles created once its baryonic density and temperature reach the hadronic phase.

[2] Often also referred to as chemical potential μ.

Naturally, if one were to study the properties of a substance like e.g. H_2O one would investigate its phases. The same reasoning applies to the QGP: Mapping out the phase diagram will allow us to study quarks and gluons directly as they are described by QCD.

2.2.2 Nuclear Modification Factor R_{AA}

It is very common in heavy ion studies to compare an observable Ψ_{pp} measured in pp collisions to the same quantity measured in pA or AA collisions with respect to the centrality described by the impact parameter b, pseudo rapidity η[3], center-of-mass energy $\sqrt{s}$, momentum transverse to the beam axis p_{T} , and particle type (by mass m). If this comparison is carried out by taking the ratio

$$R_{AA} = \frac{\Psi_{AA}(b, \eta, \sqrt{s}, p_{\mathrm{T}}, m)}{\langle N_{bin} \rangle \, \Psi_{pp}(b, \eta, \sqrt{s}, p_{\mathrm{T}}, m)} \tag{2.3}$$

R_{AA} (or R_{pA}, which is inferred in the following for the sake of brevity) is referred to as *Nuclear modification factor*. If no collective effects were present in AA collisions one could regard every such collision as a superposition of pp collisions (*binary scaling*). Therefore, R_{AA} would also depend on the size of the nucleus - an undesirable effect hindering comparisons. To overcome this, R_{AA} is normalized to the mean number of binary collisions between nuclei $\langle N_{bin} \rangle$. While $\langle N_{bin} \rangle$ is clearly 1 in case of pp collision it is not a trivial task to determine it for AA or pA collisions. Commonly, these values are determined by the Glauber-model. With the normalization in place, R_{AA} can either indicate a suppression ($R_{AA} < 1$) or an enhancement ($R_{AA} > 1$) of the respective observable.
The binary scaling is, however, only applicable if no collective effects are present and hence breaks down for soft parton interactions. The significance of the R_{AA} is thus limited to hard interactions above $\sim 5\,\mathrm{GeV/c}$.

2.2.3 Jet Quenching

One of the most important results in heavy ion physics is the nuclear modification factor of the charged particle density per p_{T} bin ($\frac{dN_{ch}}{dp_{\mathrm{T}}}$). Current results for pPb and PbPb collisions are presented in [2] and depicted in fig. 2.3. The pPb results are consistent with unity (binary scaling to pp) which indicates the absence of a strongly interacting medium in this collision system. The PbPb data is presented for central[4] and peripheral collisions revealing a dependence on this impact parameter while both spectra are suppressed over the entire p_{T} range. The rich structure of the PbPb spectrum indicates the presence of the QGP which is believed to cause an effect called *jet quenching*: A colored particle of high p_{T} created within the QGP will have to traverse the strongly interacting medium surrounding it. Thereby it loses energy by interacting with the colored medium and will eventually produce a less energetic jet (with smaller multiplicity) than it would have without a medium. The centrality dependence reflects that this effect depends on the size of the medium traversed: Peripheral collisions create a smaller overlap region and thus a smaller QGP (if any) compared to central collisions.

[3] Pseudo rapidity is defined as $\eta = -\ln\left[\tan\left(\frac{\theta}{2}\right)\right]$ where θ describes rotations around an axis perpendicular to the beam axis.

[4] While this parameter is naturally available in simulations it has to be inferred from the collision's multiplicity in experimental data. See sec. 4.1.3

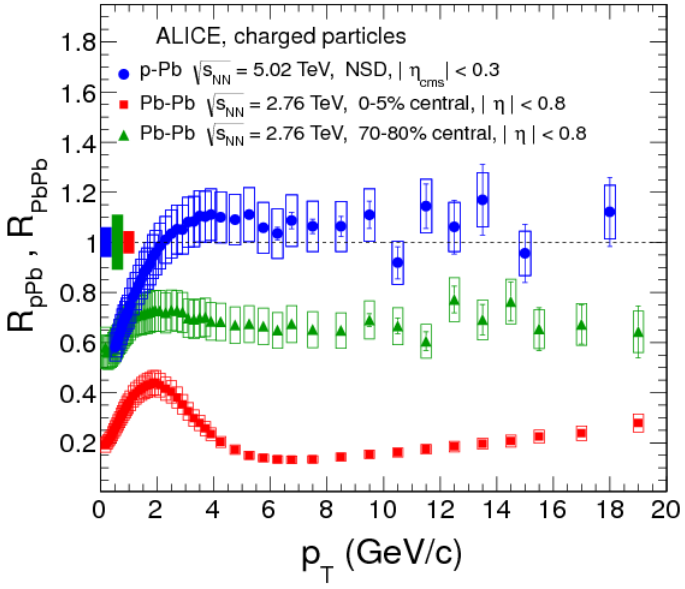

Figure 2.3: Nuclear modification factor of charged particle densities for p-Pb, central Pb-Pb and peripheral Pb-Pb collisions. p-Pb exhibits a suppression for soft events and a binary scaling for $p_T > 2$ GeV/c. The Pb-Pb results display a clear centrality dependence. From [2].

2.2.4 Quarkonium disassociation

Another fascinating effect of the QGP is the so called "melting" of exited states of quarkonium (heavy quark-antiquark pairs). Each excited state exhibits a specific binding energy and is thus expected to break at a unique temperature. Therefore, studying the suppression of these states in heavy ion collisions yields an excellent tool for probing the properties of the created matter. Such studies were carried out for the exited states of Υ ($b\bar{b}$-meson) in [12] and confirmed the expectations (cf. fig. 2.4): the exited states $\Upsilon(2S)$ and $\Upsilon(3S)$ were found to be suppressed in PbPb collision in comparison to pp collisions, again indicating the presence of a strongly interacting medium in PbPb collisions.

2.2.5 Hydrodynamic Flow

The phenomena of greatest interest for the remainder of this thesis is, however, an anisotropy in the detected particle distribution commonly referred to as *flow*. The effect is observed in the angular correlations[5] between a set of two particles which is depicted in fig. 2.5 (left). Two ridge like structures are visible, which are elongated over the entire $\Delta\eta$ region and are thus called *long-range* correlation. They indicate that the particle production in PbPb collisions is enhanced within a plane parallel to the beam axis. The orientation of this plane is different for each event, i.e. tilted by an angle φ parallel to the beam axis.
This effect can be very well described by a hydrodynamical expansion of the QGP. While the

[5] See sec. 4.2 for details on how to obtain these correlations

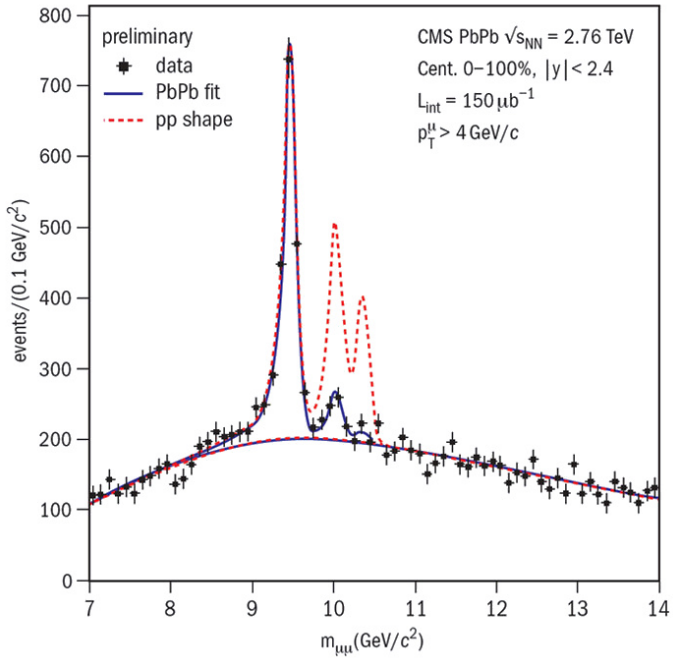

Figure 2.4: Di-muon invariant mass spectrum from Pb-Pb collisions revealing the suppression of the exited states $\Upsilon(2S)$ and $\Upsilon(2S)$ in comparison to the pp collisions. From [37].

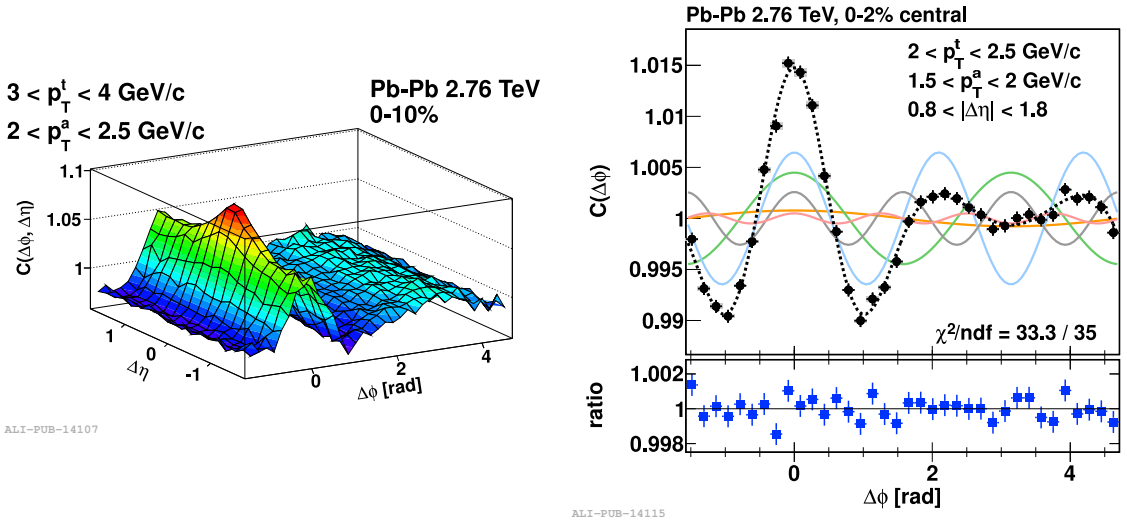

Figure 2.5: Two-particle correlation functions for Pb-Pb collisions at 2.76 TeV at $0-10\%$ centrality (left) and $0-2\%$ centrality (right). Left: The Particle production is clearly enhanced along $\Delta\varphi = 0$ and $\Delta\varphi = \pi$. Right: The two-particle correlation was projected onto $\Delta\varphi$ and decomposed into its Fourier components revealing strong contributions of triangular (blue) and elliptic (green) flow. From [4, 5].

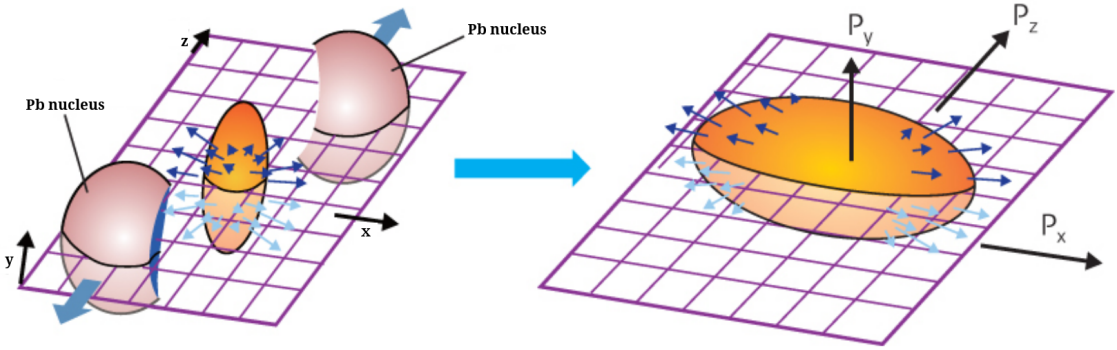

Figure 2.6: Non central collision result in a ellipsoidal overlap region. The resulting pressure gradient along the reaction plane leads to an enhancement in hadron production and p_{T} in-plane compared to out-of-plan.

previously described jet-quenching primarily depended on the size of the QGP, flow depends on its anisotropic shape. Approximating the two colliding Pb nuclei as spherical objects yields an almond shaped interaction region depending on the impact parameter. Fig. 2.6 (left) depicts such a non-central collision. The hydrodynamical model assumes that the temperature and pressure in the overlap region permit the creation of a QGP. The elliptic shape gives then rise to a pressure gradient which will boost particle production and their p_{T} within the plane depicted as a grid in the figure. This plane is known as the *reaction plane* and is tilted with respect to the laboratory's x-axis by the angle Ψ^{RP}. Assuming a near-ideal Fermi liquid (vanishing viscosity) it is then possible to model the observed azimuthal collective behavior as [40]

$$\frac{dN}{d\eta d^2p_{\mathrm{T}}} = \frac{dN}{2\pi p_{\mathrm{T}} dp_{\mathrm{T}} d\eta}\left[1 + \sum_{k=1}^{\infty} 2v_k \cos(k(\varphi - \Psi_k^{RP}))\right] \tag{2.4}$$

where φ represents the azimuthal angle and v_k is the k-th Fourier coefficient depending on η and p_{T}. If both nuclei were identical and free of fluctuations, all the odd moments of eq. (2.4) would vanish [11]. Since this is, however, a rather crude approximation, v_1 (*direct flow*) and v_3 (*triangular flow*) are indeed observed, each in their own reaction plane (angle) Ψ_k^{RP}. However, the *elliptic flow* v_2, which is responsible for the above described boost of particle production within its reaction plane, is the most dominant term in eq. (2.4) for all but the most central collisions where the almost spherical overlap region favors v_3. Fig. 2.5 (right) displays the Fourier decomposition of such central events. As anticipated, v_2 and v_3 are the most dominant components.

For the case of PbPb collisions it was found that the hydrodynamical description of the QGP is in excellent agreement to experimental observations for various centralities as well as center-of-mass energies[28]. Further experimental support for this model is given by the observation of a significant momentum anisotropy for both, light and heavy, hadrons [17]. This suggests a collective behavior of quarks of various flavors prior to hadronization.

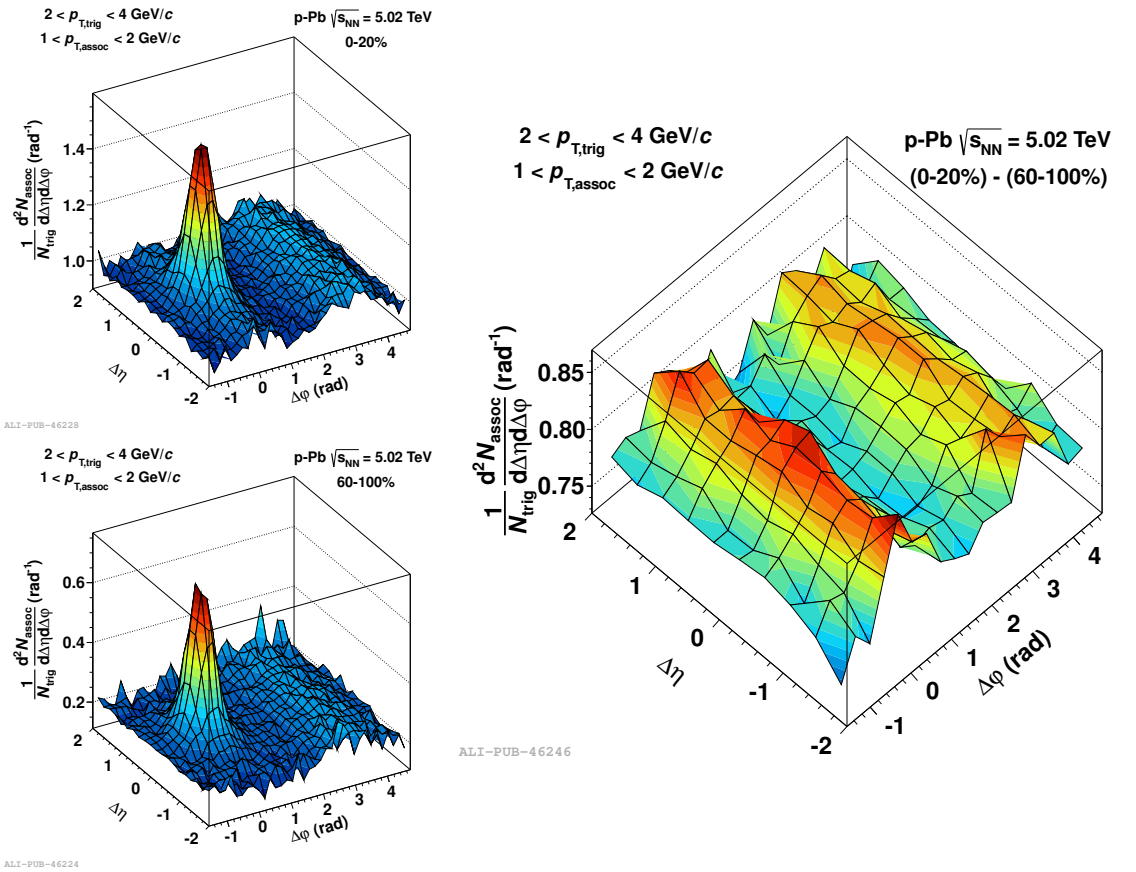

Figure 2.7: Extraction of the double-ridge structure from pPb measured data at $\sqrt{s} = 5.02\,\text{TeV}$ by calculating the two-particle correlations of high (top left) and low (bottom left) multiplicity events separatly. A subtraction of the two reveals the presence of a flow-like effect in the high multiplicity events. From[22, 24, 23].

2.3 Flow like observations in p-Pb collisions

It should be emphasized that the hydrodynamic model and the subsequent hadronization is a soft process based on collective behavior of a bulk of strongly interacting particles. It can only be applied if a QGP-like medium was formed and if an initial anisotropy is present. While both of these requirements are reasonably likely to be fulfilled in PbPb collisions this cannot be said in the case of pPb collisions. Nevertheless, as shown in this thesis as well as in [1], a so-called *double-ridge* structure can be found in high multiplicity pPb collisions. The full procedure for the extraction of this double ridge is exhaustively explained in chapter 4 but may be summarized (and simplified) as follows: At first, two-particle correlations are calculated for low and high multiplicity events separately (cf. fig. 2.7 top left and bottom left). Both of these correlation functions are dominated by the di-jet component from hard interactions which, it is conjectured, can be removed by subtracting the low multiplicity histogram from the high multiplicity one (fig. 2.7 (right)). This procedure reveals that a flow like double ridge structure is present in high multiplicity events.

The observation of these long-range $\Delta\eta$ correlations was not anticipated but is of great interest and has likely wide ranging consequences for the further understanding of QCD effects. Several theoretical explanations have been proposed ranging from final state effects, such as the above described hydrodynamical expansion, to initial state effects modeled by the Color Glass Condensate (CGC) and to hadronization "cross talk" between independent partonic collisions described by *Color Reconnection*.
The hydrodynamical model is based on the QGP and was described above; the latter two models will be introduced in the following.

2.3.1 Color Glass Condensate and Glasma

The CGC is a framework for describing the initial states of the colliding hadrons at ultra-relativistic energies. A thorough introduction is presented in [21]. Firstly, it takes into account the Lorentz contraction of the nuclei which makes them appear essentially as two dimensional planes in the laboratory frame. Secondly, all the processes which take place within the hadron exhibit a strong time dilation. This makes the partons unlikely to interact with each other during the collision; thus they may be regarded as free. The time dilation does, however, also affects the random fluctuations within the hadron, extending their lifetimes over the duration of the collision. Thus, the gluon density within the nuclei increases with increasing center-of-mass energy. The energies reached by the LHC are sufficiently large that the gluons are the main constituents.
Giving this description of the initial states the name of the theory seems aptly: *Color* refers to the color charge of the gluons in the sheets. *Glass* describes the comparably slow time evolution of the constituents and *condensate* refers to the high particle density [40]. This description only applies below a certain momentum scale denoted *saturation momentum* Q_S. For momentum transfers much larger than this scale individual gluons can again be resolved.
The collision of two nuclei in this framework is depicted in fig. 2.8 (left). In the model of CGC the two contracted nuclei pass through one another creating a form of matter called *glasma* in between them. If the energy and particle density is large enough, the glasma can produce the QGP which may than be subsequently described by the hydrodynamic model.
However, as stated above, it is not at all certain that a QGP is created in p-Pb collisions. Thus, an alternative evolution of the glasma yielding a flow-like structure in central collisions is required. In [19] the authors claim to have found such a process, or rather the combination of two, recreating the observed p-Pb phenomena. Both processes, sketched in fig. 2.8 (right), are based on gluon interferences and are referred to as *glasma graphs* and *Balitsky–Fadin–Kuraev–Lipatov (BFKL) dynamics*. The latter describes the di-jet contributions which are only very weakly dependent on the events multiplicity and thus cancel each other when subtracting the two multiplicity classes. The former, on the other hand, yields the elliptic flow like contribution with its symmetry around $\Delta\varphi = \pi/2$ for high multiplicity events.

2.3.2 Color reconnection

Both the hydrodynamical and the CGC model rely on the creation of a medium (either QGP or glasma) immediately after the collision which in its own is still disputed. Even if such a creation takes place it arises certain contradictions: eg. The interaction of a particle with a medium requires

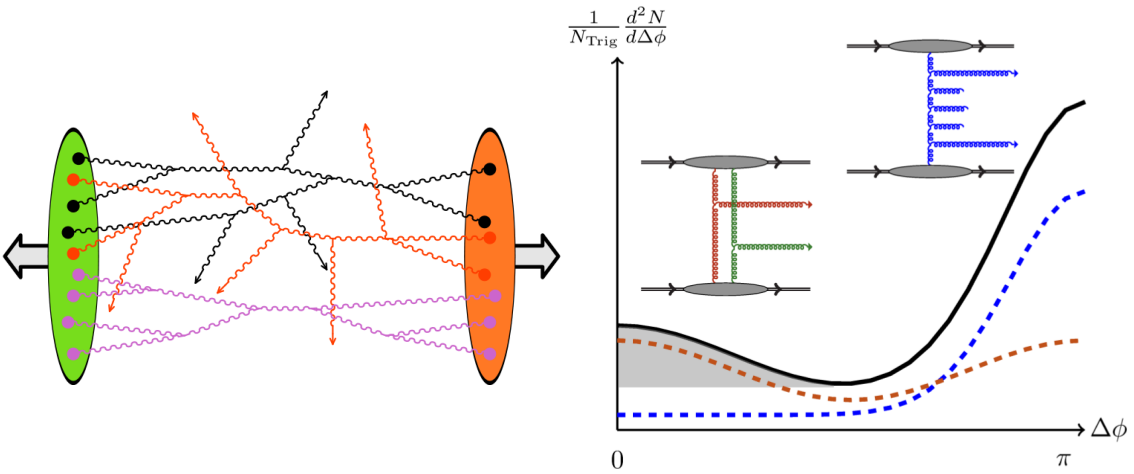

Figure 2.8: Sketch of a di hadron collision in the color glass condensate picture. Left: Two Lorentz contracted nuclei pass through each other in a collision creating a glasma between each other. Right: The BFKL theory yields a di-ject structure (blue) while the glasma-graph produces a multiplicity dependent double ridge (red). The observed combination of the two processes is shown in black. From [18, 21].

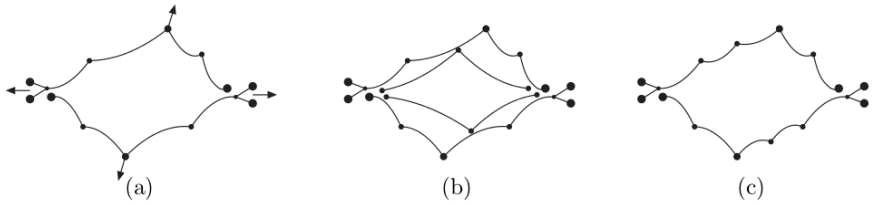

Figure 2.9: Illustration explaining the Color Reconnection taking place for two colliding nuclei. (a) depicts a single hard scattering where the outgoing partons are still color connected to the remnants of the nuclei. Two independent hard scatterings are shown in (b). (c) presents the color reconnected strings. (From [25])

that the mean free path is smaller than the system size. Hence, a model describing collective effects while not relying on a strongly interacting medium is desirable. Such an approach is proposed in [31] based on previous work (see references): Flow like effects in events with multiple hard subcollisions may be produced by minimizing the length of *Lund color strings* by reconnecting final parton from independent hard scatterings.
The effect, labeled as Color Reconnection (CR), is schematically described in fig. 2.9. (a), which depicts a possible string connection for a single hard scattering between two nuclei. The mid-rapidity, back-to-back created partons experience only a small rapidity boost since they are still connected to the remaining nuclei. If, however, multiple hard scatterings were to occur (fig. 2.9b), the strings can reconnect in a way to minimize the total string length (fig. 2.9c). This reconnection also minimizes the connection to the remaining nuclei and thus increases the mid-rapidity boost of the scattered partons.

Fig. 2.10 depicts the dependence of $\langle p_{\mathrm{T}} \rangle$ on the charged particle multiplicity N_{ch} for experimental

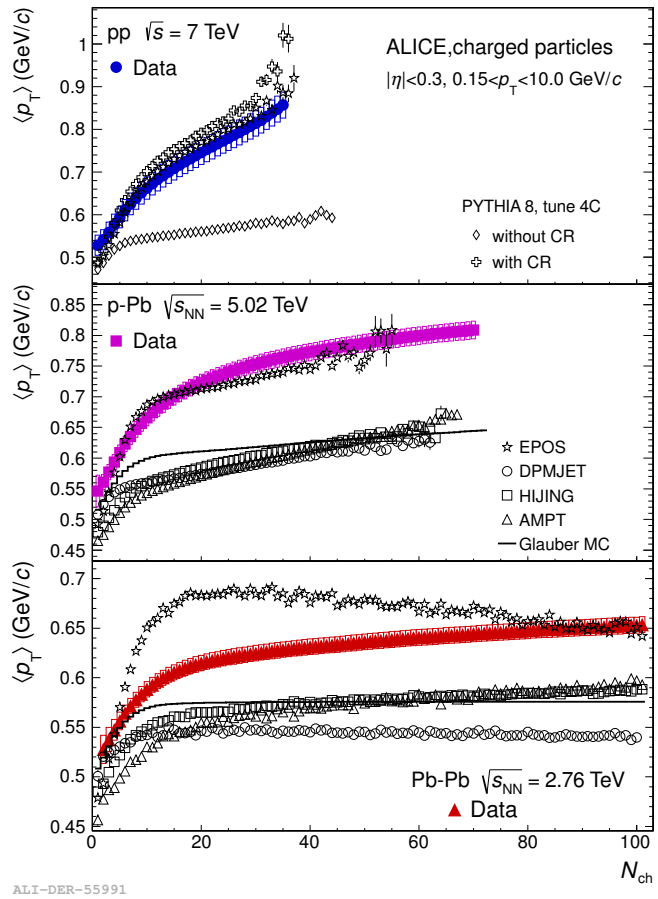

Figure 2.10: Mean transverse momentum $\langle p_{\mathrm{T}} \rangle$ as a function of charged particle multiplicity N_{ch} for pp pPb and PbPb collisions in comparison to various models. The Color Reconnection performed competitively to the hydrodynamics based EPOS model. From [8].

data as well as various event generators for pp, pPb and PbPb. The hydrodynamic based EPOS generator was able to reproduce the pPb and pp data to a high degree which is surprising since it is based on a hydrodynamic model which should not hold in these systems. Results from the PYTHIA event generator with CR are not yet available for pPb but this generator was also very successful in describing the pp data. However, in contrast to EPOS it did not contradict its underlying model in the process. Of all the listed generators only EPOS and PYTHIA with CR yield the potential to reproduce the double ridge in pPb data. Hence, this is a strong motivation to further investigate the possibility of applying CR to pPb collisions.

2.3.3 Investigating the Double Ridge in Soft and Hard Events

It is important to note that all of the above proposed explanations have fundamentally different concepts if and what medium is created in the collisions. The hydrodynamical model depends on the presents of the QGP, the CGC of its glasma and the CR expects no medium at all. Thus, these

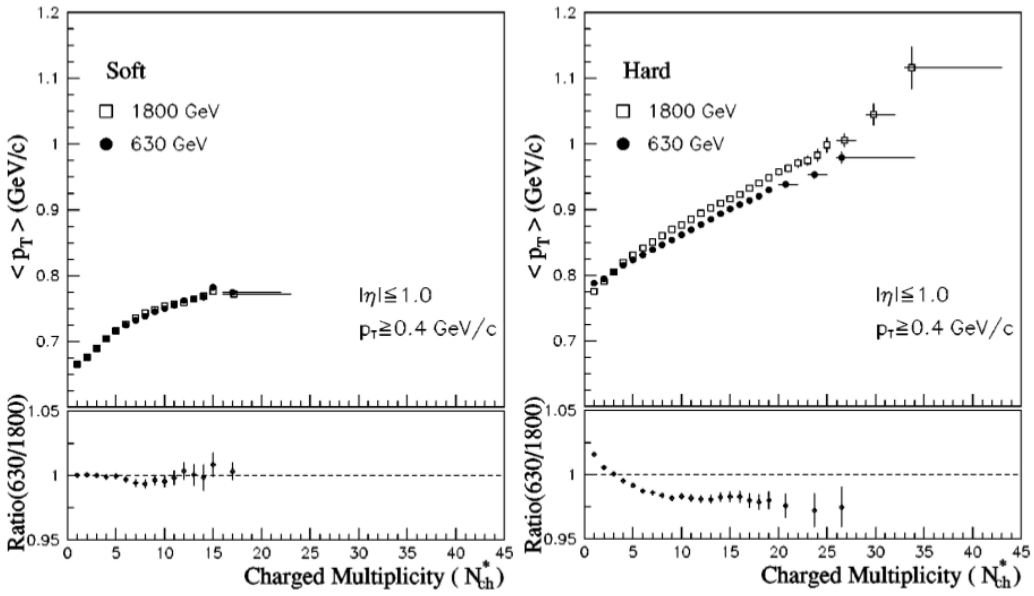

Figure 2.11: Mean transverse momentum $\langle p_{\mathrm{T}} \rangle$ vs. charged particle multiplicity N_{ch} at center-of-mass energies $\sqrt{s}$ of 630 GeV and 1800 GeV. The event sample was divided into soft (left) and hard (right) events each exhibiting distinct results. From [3].

theories are in principle mutually exclusive and it is of great importance to falsify or confirm any of these models.

As discussed in sec. 2.1.3, it is common to refer to individual subcollisions or particle tracks as *hard* and *soft* but this classification may also be applied to entire events. [3] studied antiproton-proton ($\bar{\mathrm{p}}\mathrm{p}$) collisions while applying such an event discrimination. An event was classified as hard if a single calorimeter cluster was above 1 GeV transverse energy (E_{T}) and soft otherwise. The analysis revealed large differences between the two samples. Fig. 2.11 displays the $\langle p_{\mathrm{T}} \rangle$ as a function of charged particle multiplicity for different center-of-mass energies $\sqrt{s}$. The shape of the distributions as well as the scaling with $\sqrt{s}$ are evidently dependent on the soft and hard event classification.

A similar disjunction of the event sample was carried out in this analysis probing the dependence of the double ridge structure on the hardness of the underlying events. The three discussed models are expected to behave as follows under the introduction of a bias towards harder events:

Hydrodynamical expansion is expected to show no dependence on the hardness of an event since the underlying QGP is a soft effect and will not interact with hard high p_{T} particles.

Glasma is only descriptive of interaction with momentum transfer below the saturation value Q_S which lies in the range of 1.6 to 1.9 GeV/c. Thus, the glasma should not show a dependence on the hardening of the event sample either.

Color Reconnection on the other hand, is a process build around the interplay of hard interactions. Thus, if CR is responsible for the observed double ridge in pPb data, one can expect modifications of it by biasing the event sample to harder events.

Chapter 3

The ALICE detector at the LHC

Founded in 1954, the Conseil Européen pour la Recherche Nucléaire (CERN) research facility in Switzerland was Europe's first scientific joint venture and is now counting 20 member states. CERN is dedicated to fundamental particle physics research and houses the world's largest particle collider, the LHC.

3.1 The Large Hadron Collider

The LHC is a circular particle accelerator situated in the 27 km circumference tunnel of the former Large Electron–Positron Collider (LEP) experiment. The operation of the LHC requires several pre-accelerators and is depicted in fig. 3.1. Initially, protons or Pb ions are accelerated via a linear accelerator and three consecutive synchrotron accelerators. Upon feeding the beam into the final LHC ring it is split up into two beams, one circulating through the LHC tunnel in a clockwise and the other one in a counter-clockwise direction. The two beams intersect at four specific locations each being the site of one of the four LHC experiments: A Toroidal LHC Apparatus (ATLAS), A Large Ion Collider Experiment (ALICE), Compact Muon Solenoid (CMS) and Large Hadron Collider beauty (LHCb). Each of these experiments has a specific physical main focus and its own independent collaboration associated to it. The analysis at hand is based on the data collected by the ALICE detector. Hence, only that detector is described in more detail in the following section.

3.2 ALICE

ALICE is the single dedicated heavy-ion experiment at the LHC and is built by a collaboration of 105 institutes in 30 countries [14]. It focuses on the QCD sector of the SM described in section 2.1. A detailed description of the ALICE detector can be found in [14] whilst the most important aspects are summarized in this chapter. The detector itself measures $16 \times 16 \times 26\,\mathrm{m}^3$ and weighs approximately $10\,000\,\mathrm{t}$. The center of the experiment is situated $44\,\mathrm{m}$ under ground. ALICE was planed with Particle Identification (PID) in mind while focusing on the mid rapidity region. Additionally, it was designed in anticipation of the high particle multiplicities expected from previously

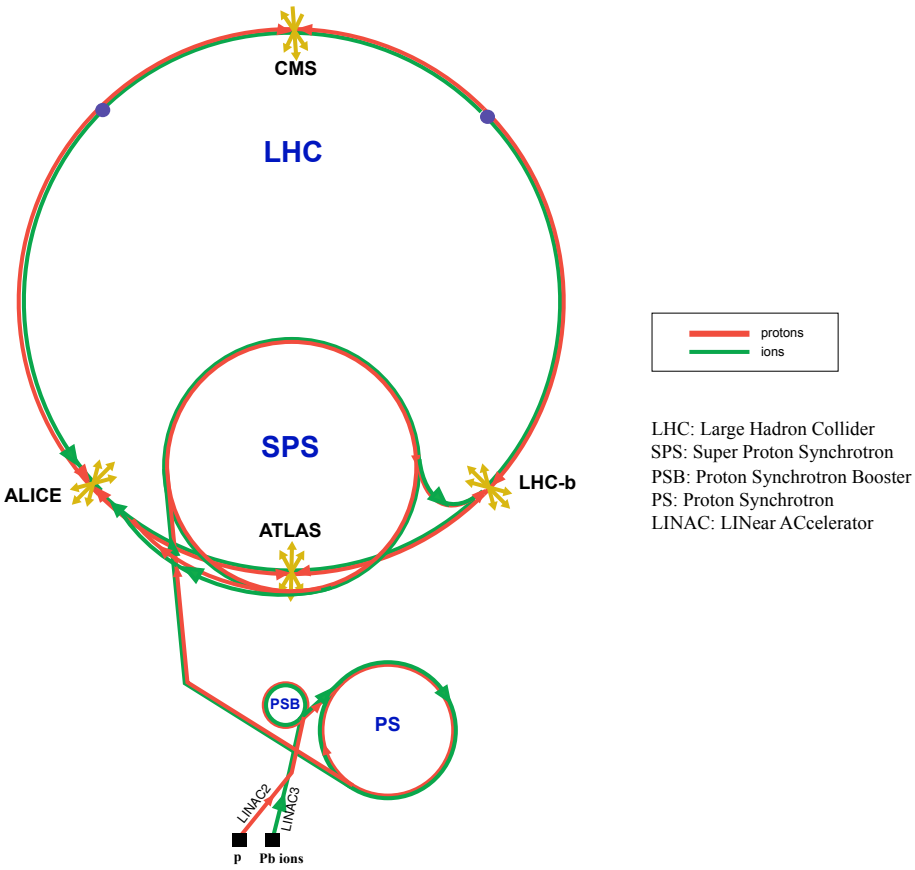

Figure 3.1: Simplified layout of the LHC, its preaccelerators and the location of the four detector sites. With modifications from [27].

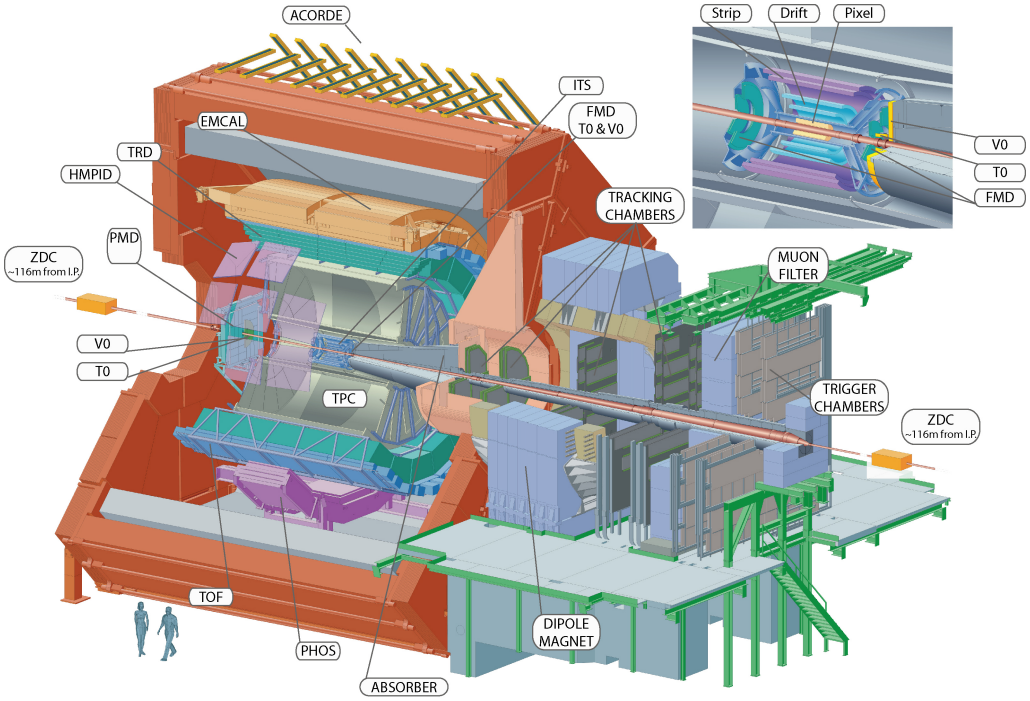

Figure 3.2: Schematic setup of the ALICE detector [35]

performed heavy ion experiments and is hence optimized for charged particle multiplicity densities of up to $dN/d\eta = 8000$ but is capable of processing twice that amount. Furthermore, ALICE possess the means to measure the particles' momenta p from several tens of MeV up to more than 50 GeV/c. The detector also records the specific ionization energy loss dE/dx, time-of-flight (TOF) information as well as transition and Cherenkov radiation. Together with the employment of electromagnetic calorimetry, muon filters and topological decay reconstruction ALICE includes essentially all known PID techniques. The particle tracking capabilities of the detector are outstanding; mainly due to the large volume of nearly $100\,\mathrm{m}^3$ and the segmentation into $\sim 500,000$ channels that are read out in 1000 time steps for each event. ALICE's data acquisition system is capable of writing 1.3 GB/s to permanent storage.

3.2.1 Detectors of importance to this analysis

ALICE is composed of several individual detector systems and is schematically depicted in fig. 3.2. The detector consists of a central barrel part (left hand side) and the muon arm (right hand side). The following discusses the components immediately involved in the here presented analysis while reference is again made to [14] for a more complete description.

Particle tracking detectors

Particle tracking is mainly achieved by the Inner Tracking System (ITS) and the Time Projection Chamber (TPC). The former (depicted in the inlay of fig. 3.2) is a six layer silicon vertex detector

situated immediately around the interaction point, it measures $97.6\,\text{cm}$ along the beam axis and has a diameter of $87.2\,\text{cm}$. The ITS is itself composed of three more detector systems; ordered by increasing distance from the beam pipe they are the Silicon Pixel Detectors (SPD), the Silicon Drift Detectors (SDD) and the Silicon mico-Strip Detectors (SSD). The main purpose of the ITS in this analysis is the localization of the primary vertex with a resolution $\leq 100\,\mu\text{m}$, an improvement of the momentum and angular resolution of the TPC and yielding a criterion for track cut selection (cf. sec. 4.1.1) However, it is also capable of measuring secondary vertices of decaying heavy hadrons and can track particles with a momentum below $200\,\text{MeV/c}$. While covering the full azimuthal angle the ITS covers a pseudo rapidity range of $|\eta| < 1.98$.
The cylindrical TPC is the main tracking detector of ALICE and completely encloses the ITS. Its active volume, filled with a mixture of Ne/CO_2/N_2, reaches from the inner radius of $\sim 85\,\text{cm}$ to the outer one of $\sim 250\,\text{cm}$ and extends parallel to the beam axis for $500\,\text{cm}$. Like the ITS the TPC covers the full azimuthal angle and a rapidity range of $|\eta| < 0.9$ if the full track length is required. The active volume is divided at its center by a aluminized Mylar foil extending perpendicular to the beam axis. In order to achieve a constant voltage gradient towards the ends of the detector of $400\,\text{V/cm}$ a high voltage of $100\,\text{kV}$ is applied to the central foil.
An electron created in the active volume by ionization yields a maximum drift time of $\sim 90\,\mu\text{s}$ until it reaches the end caps of the TPC where the readout chambers are situated. Since the track density decreases with increasing radius from the center ALICE has two different readout chambers are segmented radially into an inner and an outer readout chamber. Both of them utilize a Multi Wire Proportionality Chamber (MWPC) to amplify charges drifting towards the read out planes situated immediately underneath.
If a charged particle traverses through the active medium ionization occurs along its trajectory. The created electrons will drift at a constant velocity along the electric field towards the MWPC where they cause an avalanche of further electrons inducing a signal in the closest read out pads. This allows the two dimensional projection of the bending track to be measured. By also measuring the precise timing of these signals and knowing the constant drift velocity, it is possible to reconstruct the three dimensional trajectory of all charged particles traversing the TPC.

Triggering and multiplicity estimation

The analysis presented here relies on the V0 detector for multiplicity estimation as well as event selection. It consists of two arrays of scintillator counters, V0A and V0C, on opposite sides of the interaction point. The former is situated oppositely from the muon arm and $340\,\text{cm}$ from the vertex. It covers the rapidity range of $2.8 < \eta < 5.1$. The latter is located $90\,\text{cm}$ from the vertex while covering the interval of $-3.7 < \eta < -1.7$. The embedding of this detector in the event selection and multiplicity estimation is described in sec. 4.1.

Chapter 4

Analysis method and efficiency correction

4.1 Selection and classification of events and tracks

The selection criteria for validating events and tracks in a sample is of great importance since later measurements may be biased by these selections. The following describes which data sets were used and which conditions each event and each track had to meet in order to be considered in the further analysis. The entire analysis was developed in the *ROOT* and *AliROOT* frameworks which offer a high performance iteration through recorded events.

4.1.1 Event and track selection

The analysis is performed on the pPb collisions with a center-of-mass energy of $\sqrt{5.02}$TeV from the LHC13b and LHC13c periods with the second iteration of track reconstruction (pass2). For efficiency and closure investigations Monte Carlo (MC) generated events in period LHC13b2 (part 1-3, "efix") were used. These events were generated by the Dual Parton Model based DPMJET event generator described in [32]. DPMJET implements the Reggeon theory for simulating soft, and perturbative QCD for simulating hard events. MC events which were not exposed to any simulated detector efficiencies are referred to as MC-truth; and if they were, the are denoted as MC-reconstructed.
Valid events are required to have a signal in both the V0A and V0C detectors[1]. Furthermore, the events' reconstructed vertex positions are required to be within ± 10 cm of the detector's center along the beam axis (z_{vtx}).
This analysis focuses on tracks which are primary particles reconstructed in the ITS and TPC[2]. These tracks are commonly referred to as golden cuts tracks. In order to investigate the sensitivity of the analysis to the choice of track cuts, the so called TPC-only[3] cuts were also used in some

[1] This corresponds to the AliRoot trigger bit AliVEvent::kINT7

[2] The exact filter used was filter bit 10 corresponding to AliESDtrackCuts::GetStandardITSTPCTrackCuts2011(kTrue, 0)

[3] This corresponds to filter bit 10 or AliESDtrackCuts:GetStandardTPCOnlyTrackCuts()

instances. The difference between the tracks is that the golden tracks require associated hits in the SPD and are therefore less likely to include secondary tracks from e.g. weak decays of heavy quarks, but they have lower efficiency and an asymmetric φ acceptance due to SPD cooling issues that meant that not all sectors could be operated. TPC-only tracks are required to have a Distance of Closest Approach (DCA) to the reconstructed interaction vertex of less than $2.4\,\mathrm{cm}$ transverse and $3.2\,\mathrm{cm}$ parallel to the beam direction, while golden tracks have a p_T dependent DCA cut that is in general much tighter.

4.1.2 Enriching the sample with hard events

In order to investigate the dependence of any observable on the hardness of the underlying interaction, an additional event selection criterion was introduced. The definition of a hard event is similar to the one given in [3] and assumes that a hard parton interaction develops into a high p_T final particle. The enriched hard sub-sample is then produced by requiring at least one valid track with a p_T value above a given threshold $p_\mathrm{T}^\mathrm{thresh}$.

4.1.3 Multiplicity classes

Picturing the Pb nucleus as an extended object it is possible to define centrality as a parameter of the collision geometry. The centrality estimation used for this analysis is outlined in [29, 7].

The more central a collision is, the more binary collisions N_{coll} will occur, i.e. the centrality is given by an estimator depending monotonously on the number of collisions. Subsequently, N_{coll} is connected to the number of measurable charged particles via the Glauber model[38]. Thus the centrality of a collision may be estimated by measuring its number of charged tracks N_{ch}. Much work has been ongoing in ALICE to link multiplicity to centrality, but this is not yet quantitatively well understood for pPb collisions. The problem arises from the relatively large fluctuations (in comparison to PbPb) in N_{ch} for a fixed value of N_{coll} causing different detectors to have different biases [29].Thus throughout the following, the more general term “multiplicity” will be used instead of the debated and more model-dependent “centrality”. Nevertheless, the two terms describe essentially the same property of an event.

As presented in sec. 3.2.1, ALICE has a number of detectors capable of measuring multiplicities covering various pseudo-rapidity ranges. Commonly, the total charge deposited in either one or both of the V0 detectors is used to deduce the multiplicity of the underlying event. If the sum of V0A and V0C is used in the multiplicity determination, the method is referred to as *V0M*; if only the counts yielded by VZEROA are processed, the estimator is also called *V0A*. The latter one was used in this analysis.

In order to study the multiplicity dependence of two-particle correlations, four event classes were defined as ranges in the measured multiplicity. The classes are labeled according to the sections in the distribution of the number of events detected with each such multiplicity. This distribution is depicted in fig. 4.1. Hence, the classes are labeled as $(0-20\%)$, $(20-40\%)$, $(40-60)\%$ and $60-100\%$; the first exhibiting the highest, the last the lowest multiplicity.

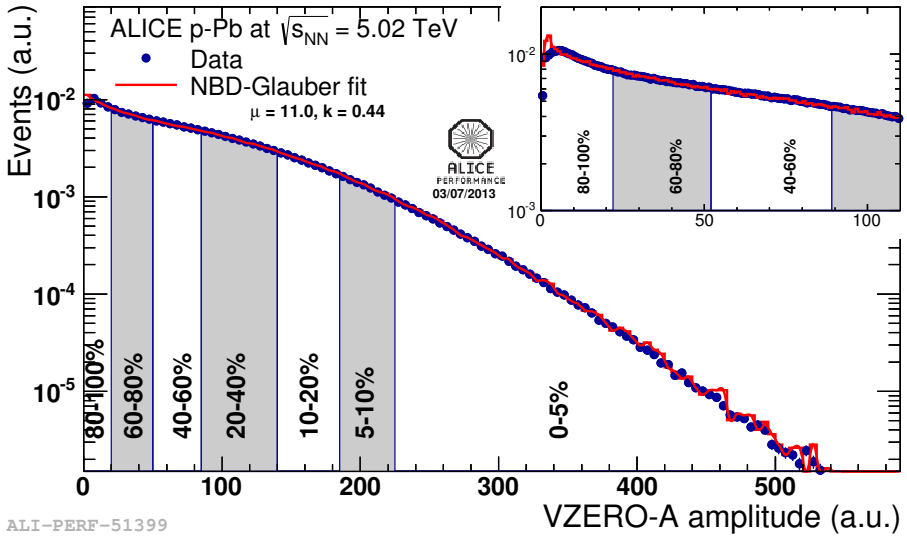

Figure 4.1: Distribution of the total deposited charge in the VZEROA detector per event. Multiplicity classes are defined as percentile of this distribution. Simulated data from the Glauber model is shown in red. From [36]

4.2 The correlation function

Two-particle correlation functions are a popular tool to investigate the structure and properties of the created medium in heavy ion physics. These correlations reflect direct correlations due to e.g. particles originating from the same jet, but may also contain indirect correlations like the flow correlations in heavy ion collisions where particles are correlated through the event planes. The aim of the here presented method is to remove the direct hard component in order to facilitate further studies of the double-ridge structure described in sec. 2.3 that can shed light on its unknown origin.

In the following analysis, the two-particle correlations are not calculated for all tracks produced by an event. Instead, two p_{T} intervals, namely a *trigger* and an *associated* interval, are defined. The transverse momentum of a particle of the former interval is denoted by $p_{\mathrm{T}}^{\mathrm{trig}}$ while the latter one is referred to as $p_{\mathrm{T}}^{\mathrm{asso}}$. Correlations are extracted from an event by calculating the azimuthal ($\Delta\varphi$) and pseudo-rapidity ($\Delta\eta$) differences between each trigger and the associated particles.

4.2.1 Signal distribution

The correlation function $S(\Delta\eta, \Delta\varphi)$, from here on denoted as *signal distribution*, for an ensemble of N_{events} events is then defined as

$$S(\Delta\eta, \Delta\varphi) = \frac{1}{\sum_{N_{\mathrm{events}}} N_{\mathrm{trig}}} \sum_{N_{\mathrm{events}}} \sum_{N_{\mathrm{trig}}} \frac{d^2 N_{asso}^{same}}{d\Delta\eta d\Delta\varphi} \tag{4.1}$$

where N_{trig} (N_{asso}^{same}) denote the number of trigger (associated) particles per event. Computing $S(\Delta\eta, \Delta\varphi)$ from experimental data will not, however, immediately yield a correlation distribution

similar to the one shown in fig. 2.7 (left), which is a corrected signal distribution know as the *total associated yield* described in sec. 4.2.3. Instead $S(\Delta\eta, \Delta\varphi)$ exhibits a triangular shape along $\Delta\eta$ as shown in fig. 4.2a. The origin of this distortion lies in the finite acceptance within the limits $\pm\eta_m$ of the detector. A trigger found at $\eta = 0$ may contribute to the signal distribution within the $\Delta\eta$ interval $[-\eta_m, \eta_m]$, while a trigger found at $\eta = -\eta_m$ may only contribute within the range of $[-2\eta_m, 0]$. Thus, any trigger may contribute to the signal at $\Delta\eta = 0$ but the number of triggers contributing to non central regions of $S(\Delta\eta, \Delta\varphi)$ decreases linearly[4] with $\Delta\eta$ yielding the triangular shape of $S(\Delta\eta, \Delta\varphi)$. It is important to emphasize that a perfect detector with infinite acceptance in η would indeed yield a $S(\Delta\eta, \Delta\varphi)$ similar to the ones shown in fig. 2.7 (left). Furthermore, no such acceptance-based distortions are expected along $\Delta\varphi$ due to the full azimuthal acceptance of the detector in practice.
The next two sections discuss the correction of this distortion which is necessary to isolate the underlying genuine correlations.

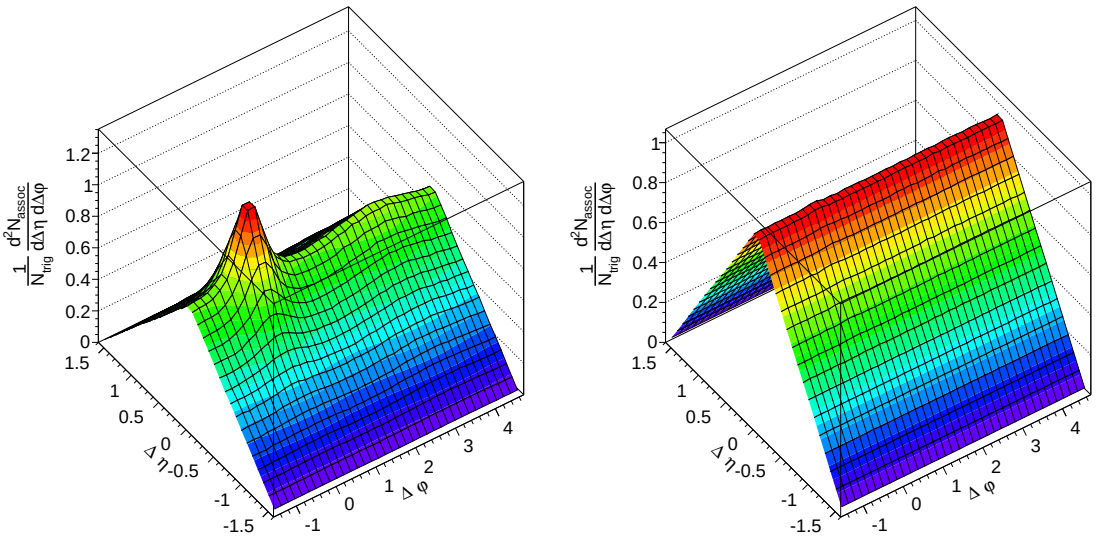

(a) Signal distribution example **(b)** Background distribution example

Figure 4.2: Examples of signal and background distributions from experimental data in the trigger (associated) interval of $1 < p_{\mathrm{T}}^{\mathrm{asso}} < 2\,\mathrm{GeV/c}$ ($2 < p_{\mathrm{T}}^{\mathrm{trig}} < 4\,\mathrm{GeV/c}$) for golden track cuts. The distributions appear distorted along $\Delta\eta$ mainly due to small differences in pseudo rapidity being accessible to a greater amount of trigger-associated pairs than large $\Delta\eta$ values.

4.2.2 Background distribution

The acceptance is indeed the main contribution to the discussed distortions (referred to as *Background* $B(\Delta\eta, \Delta\varphi)$ in the following) but not the sole. In order to correct $S(\Delta\eta, \Delta\varphi)$ for any non physics related distortions it is crucial to understand their origins. A analytical description of

[4] In fact it is not quit lineary as discussed in the following section

$B(\Delta\eta, \Delta\varphi)$, which is in fact an *autocorrelation* function, will be presented first. Subsequently, the data-driven approach for extracting $B(\Delta\eta, \Delta\varphi)$ which was applied in the latter studies will be introduced.
The following focuses on the $\Delta\eta$ variable, but all arguments are also applicable to the $\Delta\varphi$ coordinate. Firstly, it is helpful to analytically define the former mentioned detector acceptance as:

$$a(\eta) = \begin{cases} 1 & \text{if } |\eta| < \eta_m \\ 0 & \text{everywhere else} \end{cases} \tag{4.2}$$

i.e. particles within the cuts are included and all particles outside the cuts are excluded.
The next source of autocorrelations to be discussed stems from the detector efficiency ϵ which in general dependents on η (see sec. 4.4.1 for a thorough discussion of ϵ). Its effect on the two-particle correlation function may be illustrated as follows. If two regions of the detector were to exhibit a higher efficiency than all other regions, it is easy to picture that the $S(\Delta\eta)$ will show an enhancement at $\Delta\eta = 0$ and for the angular distance $\Delta\eta$ between these two regions.
Lastly, the same argument as for the efficiency may also be applied to the particle density $dN/d\eta$. Two regions with of enhanced particle density would again yield an increased correlation at $\Delta\eta = 0$ and at the angular distance between the two regions.

Having identified these three sources for the distortion of $S(\Delta\eta, \Delta\varphi)$ one can now define $B(\eta)$ in the following way [41, 34]:

$$B(\Delta\eta) \propto \int_{-2\eta_m}^{2\eta_m} d\eta f(\eta) f(\eta - \Delta\eta) \tag{4.3}$$

$$f(\eta) = a(\eta) \cdot \epsilon(\eta) \cdot \frac{dN(\eta)}{d\eta} \tag{4.4}$$

Assuming that $\epsilon(\eta)$ and $dN/d\eta$ are constant, eq. (4.3) would yield the simplified picture of a triangular shape described in sec. 4.2.1. As stated initially, the same arguments hold for the $\Delta\varphi$ variable, the only difference being that the acceptance and particle density are constant within the integration region. An example of a $B(\Delta\eta, \Delta\varphi)$ as it was used in the latter analysis is shown in fig. 4.2b.

$B(\Delta\eta, \Delta\varphi)$ could now be constructed from the measured particle density $dN/d\eta$, the known detector acceptance and an efficiency derived from MC detector simulations. This approach is very complex and error prone and an alternative way of retrieving $B(\Delta\eta, \Delta\varphi)$ purely from measured data exists. It is based on the idea that $S(\Delta\eta, \Delta\varphi) \propto B(\Delta\eta, \Delta\varphi)$ if $S(\Delta\eta, \Delta\varphi)$ is constructed from associated tracks which are entirely uncorrelated to the trigger particle. This can be achieved by pairing an event's trigger particles to associated ones from many other, independent events. However, close care has to be taken that all tracks involved in this *event mixing* have a similar efficiencies ϵ and particle distributions $\frac{dN}{d\eta}$. This is ensured by choosing associated particles from events within the same z_{vtx} interval and multiplicity class as the event of the trigger particle. Hence, a data-driven background distribution for N_{events} within a given multiplicity class and z_{vtx}

section can thus be expressed as

$$B(\Delta\eta, \Delta\varphi) = \alpha\alpha_{corr} \sum_{N_{\text{events}}} \sum_{N_{\text{trig}}} \frac{d^2 N_{asso}^{mixed}}{d\Delta\eta d\Delta\varphi} \tag{4.5}$$

where α is a constant normalizing the background to unity for points with maximal two-particle acceptance, i.e. $B(\Delta\eta = 0, \Delta\varphi = 0) \approx 1$. α_{corr} is a correction to this normalization described below.
N_{asso}^{mixed} denotes the number of associated tracks with no genuine correlation to the trigger particle. In practice, these associated particles are chosen from a *pool* of formerly processed events which have the z_{vtx} within $\pm 2\,\text{cm}$ of the trigger's event vertex and are of the same multiplicity class. Since the $B(\Delta\eta, \Delta\varphi)$ is a normalized distribution it is possible to decrease statistical uncertainties by increasing the number of uncorrelated associated particles. In this analysis each processed event was mixed with ten times the number of its associated tracks. Once the event mixing was completed for a given event, a random set of tracks in the pool was replaced by the associated particles of the current event.
When performing the afore mentioned normalization of $B(\Delta\eta, \Delta\varphi)$ it is important to take into account the finite bin width of the histogram; i.e. the most central bins of $B(\Delta\eta)$ have to be below unity as is depicted in fig. 4.3. This is achieved by the correction α_{corr}. Since the analytic shape of $B(\Delta\eta, \Delta\varphi)$ is not known it is approximated by the acceptance triangle given as $B(\Delta\eta)/\alpha \approx 1 - 1.0/\eta_m|\Delta\eta|$. Thus, α_{corr} is given by

$$\alpha_{corr} = 1 - \frac{\Delta\eta^{\text{width}}}{\eta_m} \tag{4.6}$$

where $\Delta\eta^{\text{width}}$ is the $\Delta\eta$ bin width used in the analysis.

4.2.3 Total associated yield

As stated above, any genuine correlation will cause a deviation between the Signal distribution $S(\Delta\eta, \Delta\varphi)$ and the background distribution $B(\Delta\eta, \Delta\varphi)$. However, it is a topic of current research [34] how the physical correlations combine with the background to yield the measured signal. This analysis follows the standard ALICE procedure described below and discusses the arguments brought forth in appendix A.1.
The signal corrected for the background is referred to as *total associated yield per trigger particle*[5] and denoted as $Y(\Delta\eta, \Delta\varphi)$. $Y(\Delta\eta, \Delta\varphi)$ is in this analysis defined within a given multiplicity class and z_{vtx} interval as

$$Y^{z_{\text{vtx}}}(\Delta\eta, \Delta\varphi) \approx \frac{1}{N_{trig}^{z_{\text{vtx}}}} \frac{d^2 N_{assoc}}{d\Delta\eta d\Delta\varphi} = \frac{S(\Delta\eta, \Delta\varphi)}{B(\Delta\eta, \Delta\varphi)} \tag{4.7}$$

This definition ensures that $Y(\Delta\eta, \Delta\varphi)$ is flat if no correlations between the trigger and associated particles are present. Fig. 4.4 depicts $Y(\Delta\eta, \Delta\varphi)$ for the signal and background distribution shown in fig. 4.2 revealing the common di-jet structure of pPb events.
Finally, all z_{vtx} intervals may be combined by a summation weighted by the number of triggers in each interval.

[5] Distribution of associated particles with respect to a trigger particle

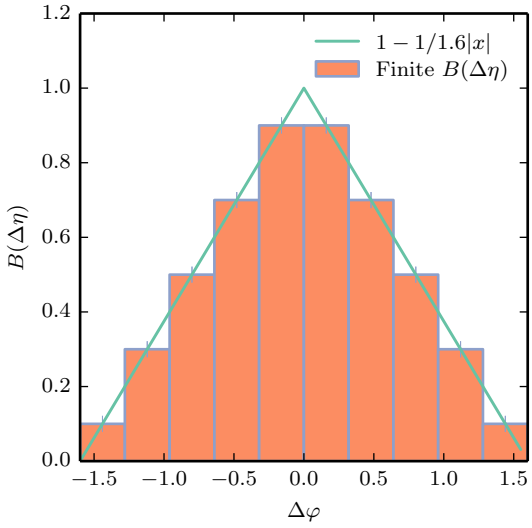

Figure 4.3: Example of the finite bin width correction as applied to the normalization of the background distribution $B(\Delta\eta, \Delta\varphi)$.

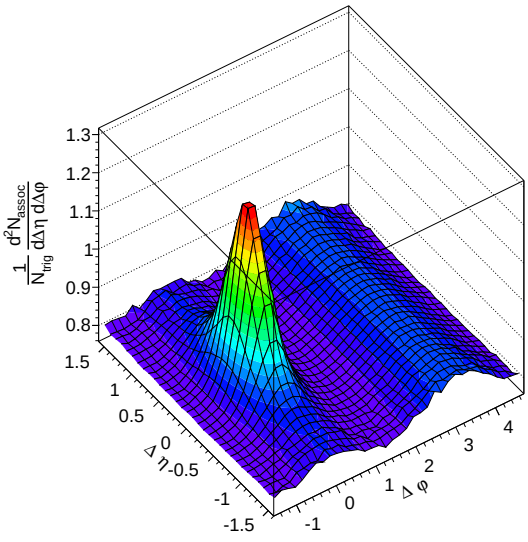

Figure 4.4: Total associated yield $Y(\Delta\eta, \Delta\varphi)$ retrieved from the distributions shown in fig. 4.2 using the definition of eq. (4.7). The di-jet structure common to pPb collisions is clearly visible.

4.3 Visual repesentation of two dimensional histograms

During the course of this project it was found that the visual representation of two dimensional histograms as depicted in fig. 4.4 may be deceiving. They do not allow for precise quantitative comparison and often it is more illuminating to examine the projections onto the $\Delta\eta$ or $\Delta\varphi$ axis. Thus, it was decided to replace the three dimensional representation seen in fig. 4.4 with a two dimensional "heat map" where "hot" (red) are high values and "cold" (blue) are low values. This has the advantage of not depending on a viewing angle while still granting a good overview of the histogram. Furthermore, this heat map shares its $\Delta\eta$ and $\Delta\varphi$ axes with projection performed onto each respective axis.
Several examples of such a combined plot, which will be used extensively in the following, may be seen in fig. 4.5. In the shown cases the $\Delta\varphi$ projection (top) was performed and averaged over the entire $\Delta\eta$ range. Chapter 5 will include instances where the *peak region* ($|\Delta\eta| < 0.8; |\Delta\varphi| < \pi/2$) was excluded from this projection. The right hand part of the combined plot shows projections onto $\Delta\eta$ for different regions of the histogram: The near-side ($|\Delta\varphi| < \pi/2$), away-side ($\pi/2 < \Delta\varphi < 3\pi/2$) and remaining regions[6]. This differentiation helps to identify and quantitatively compare $\Delta\varphi$ dependent structures in the two dimensional projection (e.g. correlations in $S(\Delta\eta, \Delta\varphi)$ as described in sec. 4.2.1).

4.4 Efficiency correction

4.4.1 Pair-efficiency correction

Depending on the cuts chosen for a given analysis, the probability of a given particle being successfully reconstructed depends on its η, φ, p_{T} and z_{vtx} . An efficiency function $\epsilon(\eta, \varphi, p_{\mathrm{T}}, z_{\mathrm{vtx}})$ can be computed from the simulated reconstruction of MC-truth events in the detector. The efficiency is then given by

$$\epsilon(\eta, \varphi, p_{\mathrm{T}}, z_{\mathrm{vtx}}) = \frac{d^4 N_{\text{mc-recon}}}{d\eta d\varphi dp_{\mathrm{T}} dz_{\mathrm{vtx}}} \Big/ \frac{d^4 N_{\text{mc-truth}}}{d\eta d\varphi dp_{\mathrm{T}} dz_{\mathrm{vtx}}} \tag{4.8}$$

where N is the total number of particles in the given collection of events. The correction is then applied by weighting each associated-trigger pair in $S(\Delta\eta, \Delta\varphi)$ and $B(\Delta\eta, \Delta\varphi)$ by $1/(\epsilon^{\text{trig}}\epsilon^{\text{assoc}})$ where ϵ^{trig} is the efficiency for the trigger particle and ϵ^{assoc} for the associated one. This method is referred to as *pair efficiency correction* in the following and represents the correction method applied in the majority of all correlation studies[34, 1]. However, the following section shows that it is possible to exploit the definition of the total associated yield per trigger particle given in eq. (4.7) in a way that replaces the entire efficiency correction procedure described above by a simple scaling of the final distribution.

4.4.2 Correction by average detector efficiency in $p_{\mathrm{T}}^{\text{asso}}$ interval

A common principle in experimental particle physics is to strive for an analysis which is as model independent as possible and does not include layers of complexity which do not improve the

[6] These definitions are used throughout the reminder of this thesis.

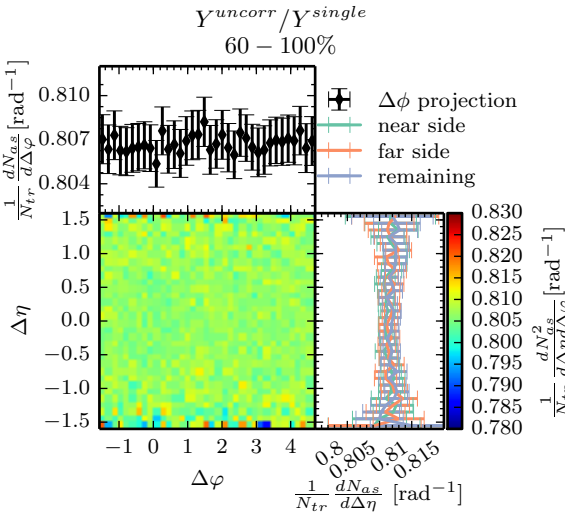

Figure 4.5: Ratio of two total associated yields per trigger particles, one computed without efficiency corrections applied, the other being corrected by a pair-efficiency correction. The obtained distribution is flat along $\Delta\eta$ and $\Delta\varphi$. The baseline of the distribution coincides well with the average detector efficiency in the given $p_{\mathrm{T}}^{\mathrm{asso}}$ interval of $0.5 < p_{\mathrm{T}}^{\mathrm{asso}} < 1\,\mathrm{GeV/c}$.

yielded results. In this spirit a new approach for treating detector efficiencies was developed and deployed during this thesis.

The starting point is eq. (4.7) which defined in this way in order to correct the autocorrelations represented by $B(\Delta\eta, \Delta\varphi)$ in $S(\Delta\eta, \Delta\varphi)$. Equation (4.4) shows that the autocorrelations stem from (generalizing to two dimensions) $\frac{d^2dN}{d\eta d\varphi}$, the detector acceptance $a(\eta, \varphi)$ and $\epsilon(\eta, \varphi)$. Assuming that the event mixing was flawless, all three of these are identical for $S(\Delta\eta, \Delta\varphi)$ and $B(\Delta\eta, \Delta\varphi)$. This means that by taking the ratio of these two quantities one corrects for all the autocorrelations caused by $\frac{d^2dN}{d\eta d\varphi}$, $a(\eta, \varphi)$ and $\epsilon(\eta, \varphi)$. Hence, the question arises what one gains by correcting the effects of the detector efficiencies individually in $S(\Delta\eta, \Delta\varphi)$ and $B(\Delta\eta, \Delta\varphi)$ as described in sec. 4.4.1 if the definition of $Y(\Delta\eta, \Delta\varphi)$ would correct for the autocorrelations caused by $\epsilon(\eta, \varphi)$ anyway? This may be illustrated by computing Y^{uncorr} from uncorrected MC-reconstructed data and $Y^{pair-corr}$ from corrected MC-reconstructed data. Fig. 4.5 shows the ratio $Y^{uncorr}/Y^{pair-corr}$ for the intervals $0.5 < p_{\mathrm{T}}^{\mathrm{asso}} < 1\,\mathrm{GeV/c}$ and $1 < p_{\mathrm{T}}^{\mathrm{trig}} < 2\,\mathrm{GeV/c}$.

As anticipated from the above discussion, no deviation from a flat distribution outside the statistical uncertainties is present. However, Y^{uncorr} is scaled by the factor ~ 0.807 in comparison to $Y^{pair-corr}$. This factor coincides with the detector efficiency averaged over the acceptance region and $p_{\mathrm{T}}^{\mathrm{asso}}$ interval to approximately $\pm 0.5\%$ in all studied intervals of $p_{\mathrm{T}}^{\mathrm{asso}}$ and $p_{\mathrm{T}}^{\mathrm{trig}}$ and even when applying the high p_{T} threshold. Furthermore, some quantities, like e.g. the v_2 are not even sensible to the error in the scaling. The ridge yields described in sec. 4.6, on the other hand, are sensible but are limited by other statistical and systematic uncertainties.

Thus, this correction method, in the following referred to as *average efficiency method*, appears

sufficiently precise and easier to apply than the pair-correction method, while also exposing the inherent independence of the two-particle correlation function onto the precise topology of the efficiency distribution and the track cuts chosen. Therefore, all of the following results were corrected by this method unless otherwise noted.

4.5 MC closure test

A closure test probes if a given correction method applied to reconstructed data yields the original MC truth results. In the case of this analysis B, S and Y were computed for the MC truth as well as for the reconstructed data. In case of the latter, the pair-efficiency correction as described in section 4.4.1 was applied to the associated tracks since a correction of $S(\Delta\eta, \Delta\varphi)$ an $B(\Delta\eta, \Delta\varphi)$ with the average efficiency method is not possible. The closure test was then performed by dividing the distributions retrieved from the reconstructed data by those based on the MC truth events.

4.5.1 MC closure test without high p_{T} threshold

Results of the MC closure test for $S(\Delta\eta, \Delta\varphi)$ and $B(\Delta\eta, \Delta\varphi)$ at $0.5 \leq p_{\mathrm{T}}^{\mathrm{asso}} \leq 1\,\mathrm{GeV/c}$ and $1 \leq p_{\mathrm{T}}^{\mathrm{trig}} \leq 2\,\mathrm{GeV/c}$ are depicted in fig. 4.6. Since the average-efficiency correction is only applicable to $Y(\Delta\eta, \Delta\varphi)$ the left hand plots were generated from uncorrected reconstructed data while the right hand ones were corrected by pair-efficiency correction as described in sec. 4.4.1. The most peripheral event class $(60 - 100\%)$ was chosen as an example since it demonstrates the strongest deviations from the MC truth. The ratio below one in the former was to be expected since the number of reconstructed associated particles per event is always less or equal to the their count in MC truth. The pair-efficiency correction is found not to lead to MC closure for S and B while introducing additional structure along $\Delta\eta$.
However, when calculating $Y(\Delta\eta, \Delta\varphi)$, which was left uncorrected (left) for the sake of comparison to fig. 4.6, these structures were found to cancel each other. As depicted in fig. 4.7, both the uncorrected as well as pair-efficiency corrected $Y(\Delta\eta, \Delta\varphi)$ showed minimal structure along $\Delta\eta$ and $\Delta\varphi$. Furthermore, the pair-efficiency corrected MC closure test yielded a baseline just $\sim 0.5\%$ above unity; i.e. the pair-efficiency correction reproduced the MC-truth data to a good approximation.
However, non-closure was observed for other intervals of $p_{\mathrm{T}}^{\mathrm{asso}}$ and $p_{\mathrm{T}}^{\mathrm{trig}}$ than the one described above. Fig. 4.8 displays the ratio of Y^{recon} and Y^{truth} for the $0 - 20\%$ (left) and $60 - 100\%$ (right) multiplicity classes. A di-jet-like structure emerged in the latter case whose origin is currently not yet understood. The non closure becomes more severe when applying a high p_{T} threshold.

4.5.2 Non closure due to event mixing

It should be noted that the entire analysis is very sensitive to the composition of the event mixing pool. Figure 4.9 shows the effects of a pool including events which do not have any trigger but are otherwise valid. Those events do not contribute to S but appear to have different particle densities $dN/d\eta$ than events with one or more triggers. Hence, following the argumentation in section 4.2.3, the resulting total yield appears distorted along $\Delta\eta$. Some other ALICE correlation analysis [34]

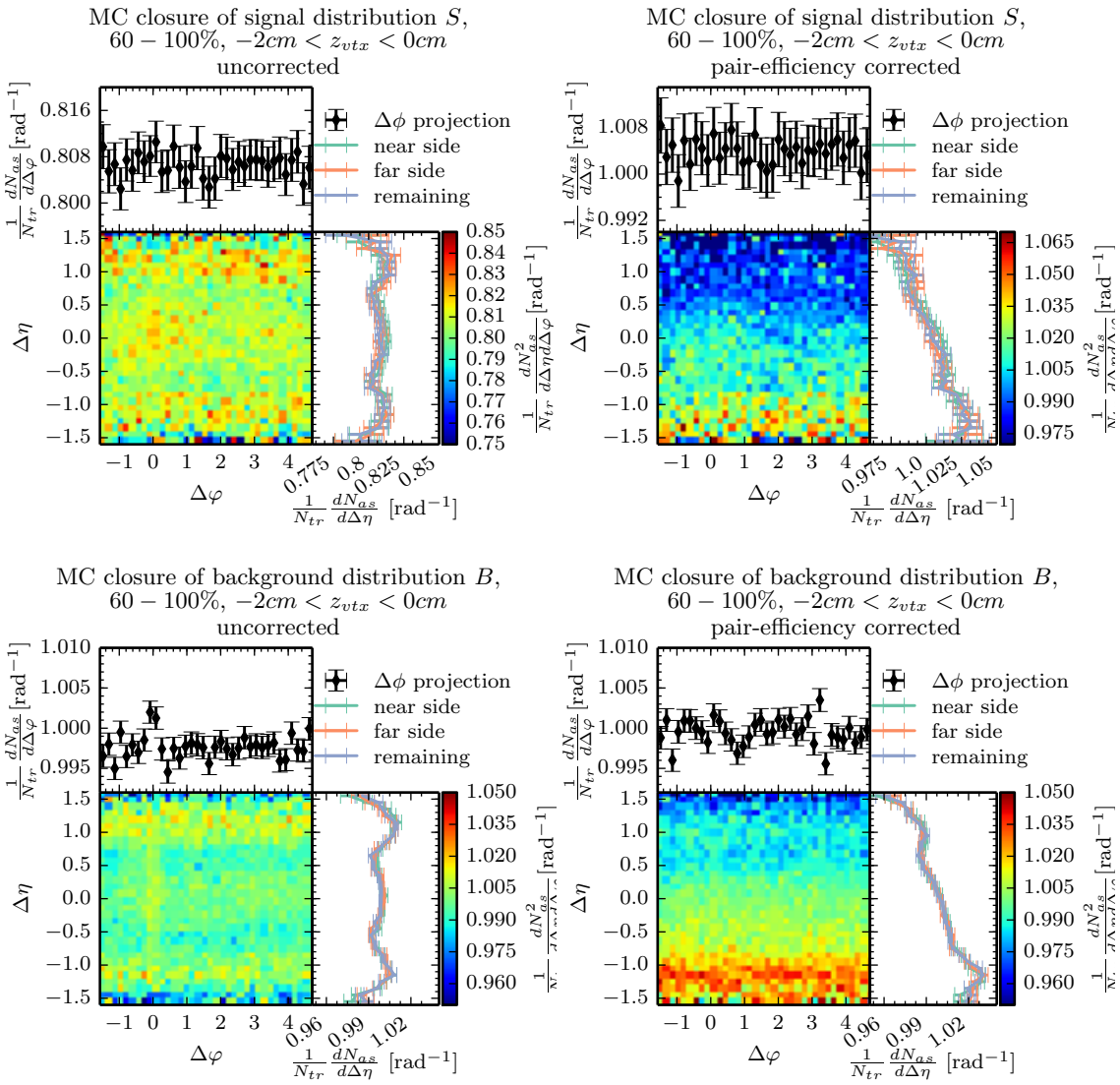

Figure 4.6: Ratios between results from reconstructed and MC truth analysis for peripheral events ($60-40\%$) at the detector center. The trigger and associated intervals are chose as $0.5 \leq p_{\mathrm{T}}^{\mathrm{asso}} \leq 1\,\mathrm{GeV/c}$ and $1 \leq p_{\mathrm{T}}^{\mathrm{trig}} \leq 2\,\mathrm{GeV/c}$. Plots on the left hand side show uncorrected results. The reconstructed data for the plots on the right hand side was corrected by pair-efficiency correction as described in sec. 4.4.1 thus representing a MC closure test. The top row shows the ratios for S, the bottom row for B. Pair-efficiency correction does not lead to closure for S and B and introduces additional structure in $\Delta\varphi$ when compared to the uncorrected ratios.

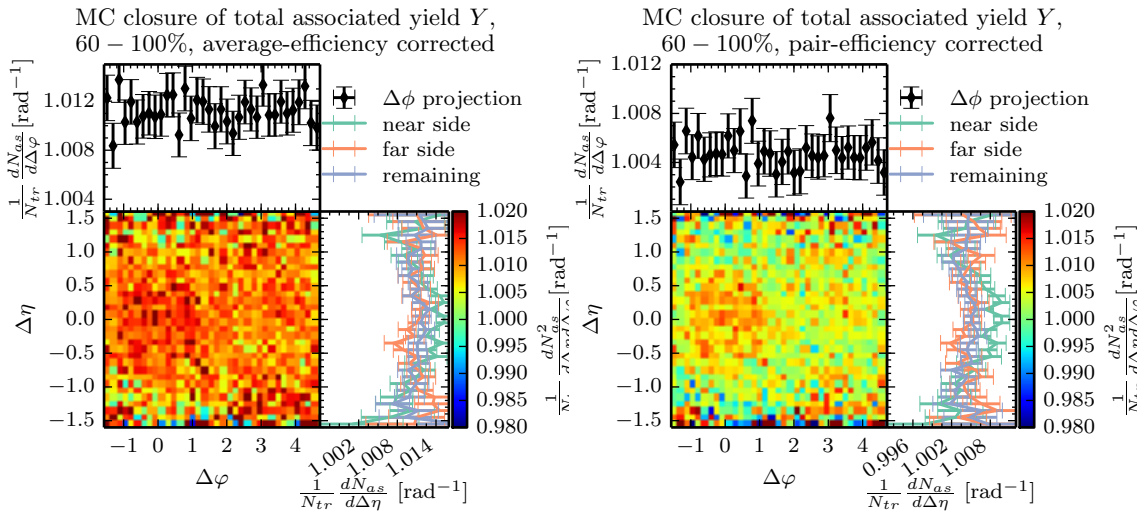

Figure 4.7: Ratios between the total associated yield Y computed from reconstructed and MC data for peripheral events $(60-40\%)$. The trigger and associated intervals were set as $0.5 \leq p_{\mathrm{T}}^{\mathrm{asso}} \leq 1\,\mathrm{GeV/c}$ and $1 \leq p_{\mathrm{T}}^{\mathrm{trig}} \leq 2\,\mathrm{GeV/c}$. The left hand plot shows the uncorrected result. The reconstructed data of the plots on the right hand side was corrected by pair-efficiency correction as described in sec. 4.4.1. The $\Delta\varphi$ structures observed in 4.6 appears to cancel when calculating Y for both corrected and uncorrected results. "Closure" may be achieved for the uncorrected data by scaling Y by a constant value.

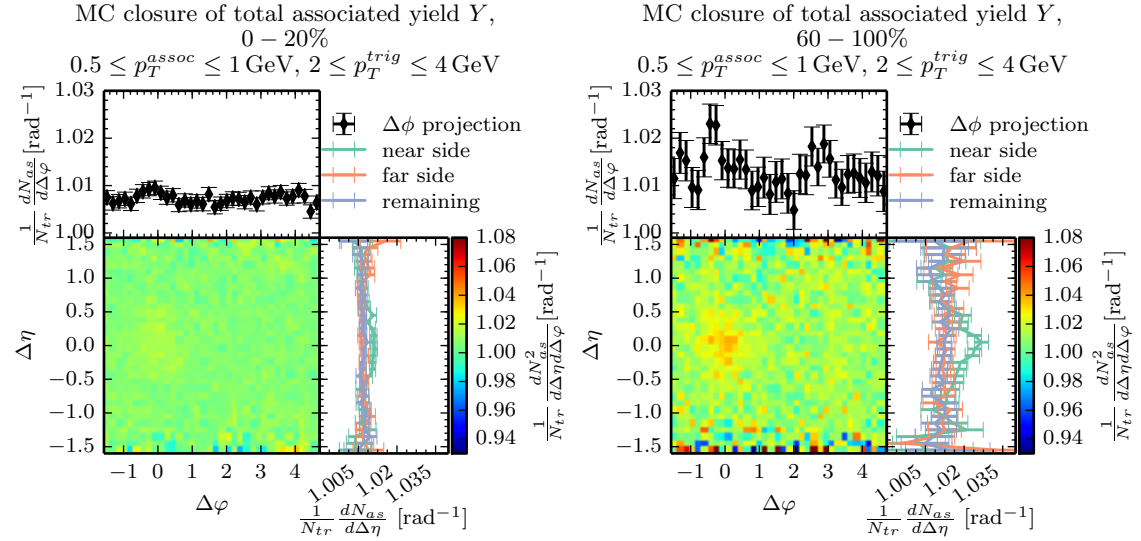

Figure 4.8: MC closure test pass for the $(0-20\%)$ class (left) and fails for $(60-100\%)$ in the associated and trigger intervals of $0.5 \leq p_{\mathrm{T}}^{\mathrm{asso}} \leq 1\,\mathrm{GeV/c}$, $2 \leq p_{\mathrm{T}}^{\mathrm{trig}} \leq 4\,\mathrm{GeV/c}$. The origin of this non closure is not yet understood.

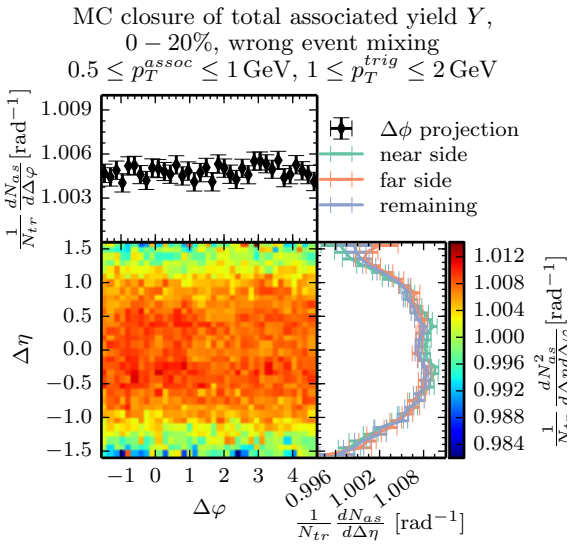

Figure 4.9: Effect of an event pool not precisely reflecting the event selection criteria of events in the signal distribution S. Events having no trigger were used in the event mixing while they were not contributing to S.

have had similar problems with so called *wings* in $\Delta\eta$ which might very well be related to such biases introduced with the event mixing.

4.5.3 MC closure with high p_T threshold

Applying the high p_T threshold $p_\mathrm{T}^\mathrm{thresh}$ as described in sec. 4.1.2 and hence dividing the event sample into soft and hard poses further complications regarding the MC closure test for the analysis method at hand. Again, it should be noted that it is crucial that the events used in the event mixing are as similar as possible to the ones use in the calculation of S. It was found that not applying the threshold criteria to the mixing events leads to a distortion along $\Delta\eta$ analogous to the one described above and depicted in fig. 4.9.
Albeit, even if $p_\mathrm{T}^\mathrm{thresh}$ is properly applied in the event mixing, MC-closure was not achieved for all event classes simultaneously in any tested $p_\mathrm{T}^\mathrm{asso}$ and $p_\mathrm{T}^\mathrm{trig}$ interval. Instead, a di-jet structure, similar to the one discussed in sec. 4.5.1, emerged for decreasing multiplicity as is shown in fig. 4.10.
The following attempts were made to understand the origin of the non closure:

- The computations were repeated for the TPC-only event cuts (golden cuts track cuts were used in fig. 4.10). As described in section 4.1.1, the former cuts are flat along φ while the latter ones exhibit significant gaps. The result for the most peripheral event class, exhibiting the most significant structure, is displayed in fig. 4.11 (left hand side). Evidently, the same di-jet like structure emerged in the TPC-only cut as was observed in golden cuts cuts. This observation is also in agreement to the considerations made when defining the average-efficiency correction in sec. 4.4.2. Hence, it can be excluded that the observed non closure originates from detector deficiencies.

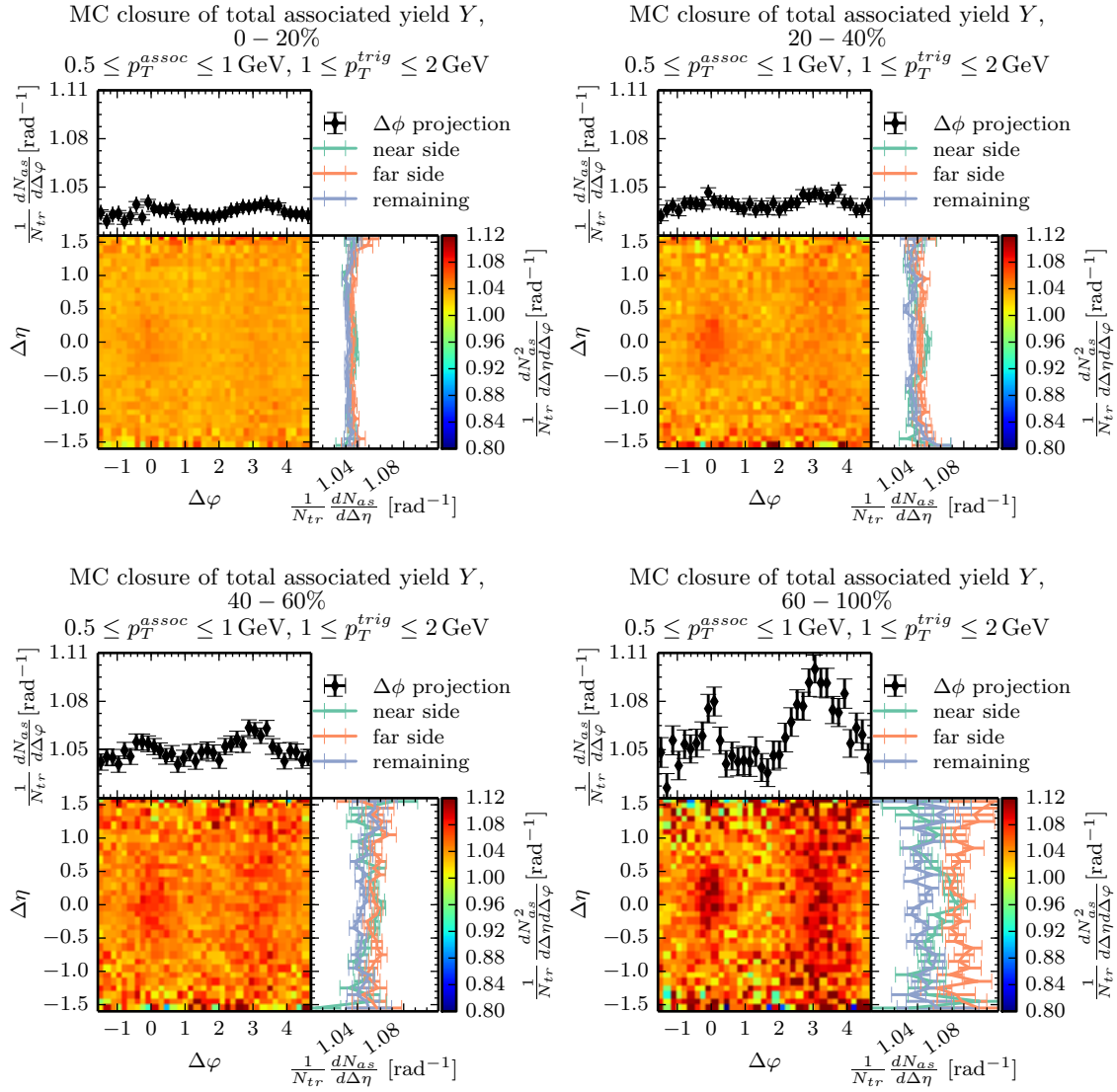

Figure 4.10: MC closure tests for all four multiplicity classes with the associated and trigger intervals at $0.5 \leq p_{\mathrm{T}}^{\mathrm{asso}} \leq 1\,\mathrm{GeV/c}$, $1 \leq p_{\mathrm{T}}^{\mathrm{trig}} \leq 2\,\mathrm{GeV/c}$ and a threshold of $4\,\mathrm{GeV/c}$. A di-jet like structure emerges with decreasing multiplicity.

- Appendix A.2 describes a bias towards events with many triggers, due to detector deficiencies and the definition of the two-particle correlation function. The effect of this bias was investigated by only considering events which have exactly one generated trigger particle at the generator level. Thus, any possible bias towards events with many triggers was eliminated. Enforcing that new requirement yielded the $Y^{\text{recon}}/Y^{\text{truth}}$ ratio shown in fig. 4.11 (right hand side). Neither the $\Delta\eta$ nor the $\Delta\varphi$ structures were significantly altered by the described limitation of the sample. Thus, the non closure seems to not stem from a event selection depending on the number of MC truth triggers in an event.

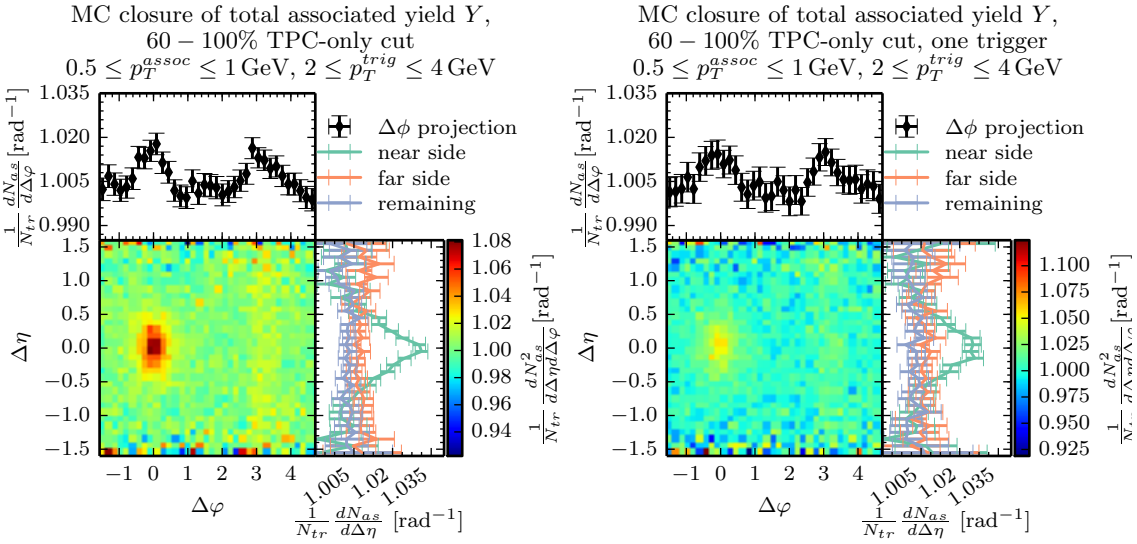

Figure 4.11: Investigation into the origin of non closure. Depicted are the cases for most peripheral events using TPC-only cuts in the associated and trigger intervals of $0.5 \leq p_{\text{T}}^{\text{asso}} \leq 1\,\text{GeV/c}$, $2 \leq p_{\text{T}}^{\text{trig}} \leq 4\,\text{GeV/c}$. Left hand side: Using TPC-only instead of golden cuts cuts leads to the same structure in $\Delta\eta$ and $\Delta\varphi$ in the closure test for both cases. Right hand side: Event selection requires exactly one trigger particle on the generator level. Again, the structure along $\Delta\eta$ and $\Delta\varphi$ remains despite this extra requirement.

Since the above attempts to illuminate the origin of the non closure proved futile, the non-closure effects were taken into detailed consideration when discussing the measured results in chapter 6.

4.6 Subtraction method

Multiplicity dependencies of Y are investigated by a simple subtraction method. Most commonly, the most peripheral case is subtracted from the most central total associated yield. Applying this procedure to the MC-reconstructed data yields a flat distribution if no high p_{T} threshold is enforced. This case is displayed for the $p_{\text{T}}^{\text{asso}}$ and $p_{\text{T}}^{\text{trig}}$ intervals of $0.5 \leq p_T^{assoc} \leq 1\,\text{GeV/c}$ and $1 \leq p_T^{trig} \leq 2\,\text{GeV/c}$ in fig. 4.12. This means that the double ridge structure described in sec. 2.3 stems from a physical process not included in the event generator.

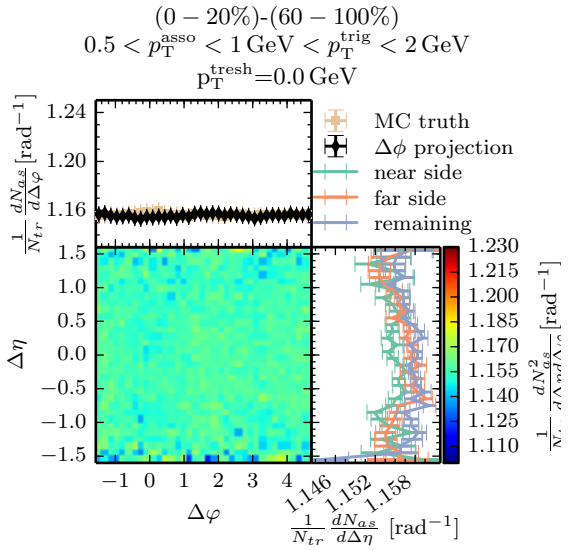

Figure 4.12: Subtracting the low multiplicity class from the high multiplicity class computed from MC reconstructed data does not yield a double ridge structure. Additionally, the same subtraction procedure was applied to MC truth data depicted in light brown in the $\Delta\varphi$ projection plot.

Also displayed in that figure are the results obtained when applying this subtraction method to the MC truth data (light brown in $\Delta\varphi$ projection plot). Originally, the baseline of $Y^{MC-truth}(\Delta\eta, \Delta\varphi)$ was enhanced in comparison to the reconstructed data by $\sim 5\%$, but was scaled to match the latter at $\Delta\varphi \approx 1.3$ rad. This allows for better comparison and further calculations described in the following. Since the combination of not enforcing a high p_{T} threshold along with the $p_{\mathrm{T}}^{\mathrm{asso}}$ and $p_{\mathrm{T}}^{\mathrm{trig}}$ intervals chosen in fig. 4.12 yielded MC closure, no discrepancy between the MC truth and MC reconstructed results is visible.
Applying the subtraction method to reconstructed data while enforcing the high p_{T} threshold yielded distributions as shown in fig. 4.13. The away-side exhibits a suppression over the entire $\Delta\eta$ range while a dip formed in the peak region. Both features become more pronounced by increasing $p_{\mathrm{T}}^{\mathrm{thresh}}$. See chapter 6 for a further discussion on the possible origin of this structure.
These two cases do not exhibit MC closure which manifests itself in the discrepancy between the MC truth and MC reconstructed data in the $\Delta\varphi$ projection. This discrepancy was used as a systematic error for the ridge yields discussed below.

Yield extraction

In order to quantify the excess between measured and reconstructed data in the subtracted distributions (i.e. the double-ridge), so-called *ridge yields* are defined. Each ridge yield covers a certain region of the two dimensional distribution. The *away side ridge* covers the full $\Delta\eta$ region and the azimuthal interval of $\pi/2 < \Delta\varphi < 3\pi/2$. The *near side yield* covers the remaining azimuthal range of $-\pi/2 < \Delta\varphi < \pi/2$ but is separated in a *peak* and a *long range* region. The former covering $-0.8 < \Delta\eta < 0.8$, the latter covering the remaining $0.8 < |\Delta\eta|$. The ridge yields are

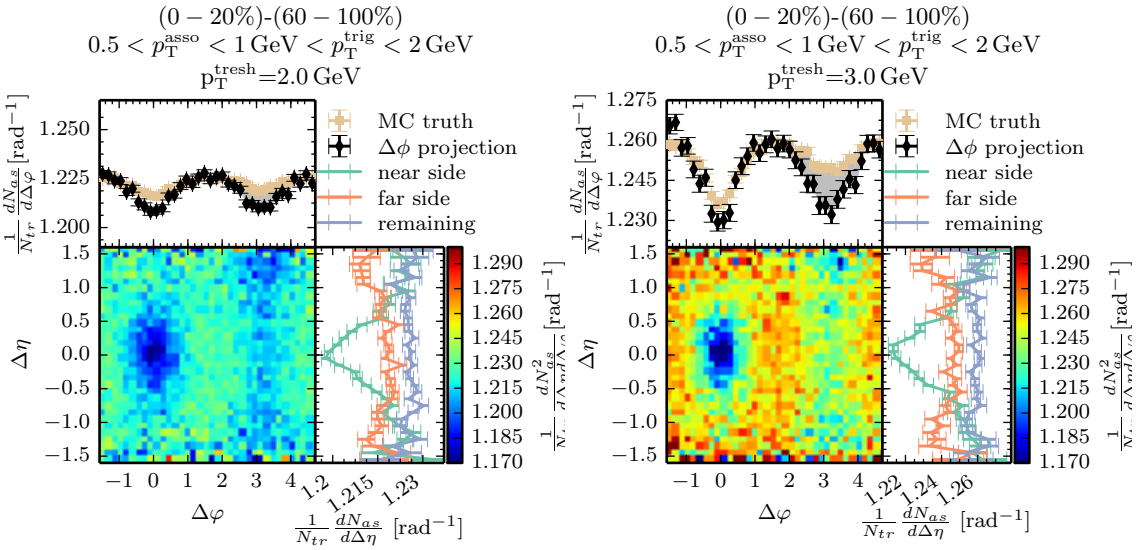

Figure 4.13: Performing the subtraction method on MC truth and MC recontructed data yields unequal results due to the non closure of the here presented method after introduction of a high p_{T} threshold. MC truth as well as MC reconstructed data exhibit a suppression on the away-side as well as a dip around the origin.

computed by integrating the respective regions in the $\Delta\varphi$ projection. The afore discussed discrepancy between the MC-truth and reconstructed data as shown in fig. 4.13 is treated as a systematic uncertainty.

Double ridge structure

Sec. 2.2.5 discussed the hydrodynamical expansion of flow like structures and its Fourier coefficients v_n. Theses quantities can be extracted from a subtraction distribution exhibiting a double ridge structure by fitting its $\Delta\varphi$ projection to

$$\frac{1}{N_{\mathrm{trig}}}\frac{dN_{\mathrm{assoc}}}{d\Delta\varphi} = a_0 + 2a_2\cos(2\Delta\varphi) + 2a_3\cos(3\Delta\varphi) \tag{4.9}$$

where the fit parameter a_0 represents the uncorrelated yield and a_2 and a_3 characterize the additional structure in the high multiplicity class. If the $p_{\mathrm{T}}^{\mathrm{asso}}$ and $p_{\mathrm{T}}^{\mathrm{trig}}$ intervals are identical it is possible to convert these parameters to the Fourier coefficients v_2 and v_3 which are more commonly used in flow studies of nucleus-nucleus collision [39]. The conversion is given by

$$v_n = \sqrt{a_n/b} \tag{4.10}$$

where the baseline b is evaluated in the region $|\Delta\varphi - \pi/2| \leq 0.2$ of the higher multiplicity distribution [1].

Chapter 5

Results

The following chapter presents the results produced by the analysis method described in chapter 4 for two different associated and trigger p_{T} intervals:
The first interval investigated is $1\,\mathrm{GeV/c} < p_{\mathrm{T}}^{\mathrm{asso}} < 2\,\mathrm{GeV/c} < p_{\mathrm{T}}^{\mathrm{trig}} < 4\,\mathrm{GeV/c}$ which was chosen because it is well documented with published results [1]. Since this analysis uses a new correction method and different track cuts[1] in comparison to former publications, it was crucial to verify the reproduction of former results. However, the high upper end of the $p_{\mathrm{T}}^{\mathrm{trig}}$ interval contradicts the intention of analyzing the softest interactions in hard events and will likely introduce a correlation between the threshold and the trigger particle. Hence, the second interval was chosen to be $0.5\,\mathrm{GeV/c} < p_{\mathrm{T}}^{\mathrm{asso}} < 1\,\mathrm{GeV/c} < p_{\mathrm{T}}^{\mathrm{trig}} < 2\,\mathrm{GeV/c}$ which fulfills the above requirements.

This chapter is divided into two parts. The first part deals with the extraction of the double-ridge structure while not requiring a high p_{T} particle in the event. The results are compared to published results where available in order to demonstrate the correct working of the average-correction method and the here used golden track cuts.

The second part of this chapter presents novel findings for events passing the additionally required $p_{\mathrm{T}}^{\mathrm{thresh}}$ criteria. Only the second interval is considered here due to the above discussed reasons.

5.1 Without high p_{T} threshold

The associated yield per trigger particle for the $p_{\mathrm{T}}^{\mathrm{asso}}$ and $p_{\mathrm{T}}^{\mathrm{trig}}$ intervals of $1 < p_{\mathrm{T}}^{\mathrm{asso}} < 2\,\mathrm{GeV/c} < 2$ and $2 < p_{\mathrm{T}}^{\mathrm{trig}} < 4\,\mathrm{GeV/c}$ are computed for the $0-20\%$, $20-40\%$, $40-60\%$ and $60-100\%$ multiplicity classes as described in chapter 4.2.3. The yielded outcome for each class is depicted in fig. 5.1. All event classes exhibit the anticipated jet peak on the near-side and a ridge like structure on the away-side including the jet recoil. A long range $\Delta\eta$ structure is clearly recognizable in the two dimension representation for the most central collisions (top left). This effect, however, diminishes with decreasing multiplicity, which can best be observed in the $\Delta\varphi$ projection excluding the jet peak region ($|\Delta\eta| < 0.8; \quad \pi/3 < \Delta\varphi < 2\pi/3$); the long-range

[1] So-called *hybrid* track cuts were used in [1]

excess on the nearside decreases in absolute value as well as in comparison to the away-side ridge.

The multiplicity dependence was further investigated by performing the subtraction method discussed in sec. 4.6 and fitting the $\Delta\varphi$ projection (excluding the peak region ($|\Delta\eta| < 0.8; \quad \pi/3 < \Delta\varphi < 2\pi/3$) to eq. (4.9). Results are displayed in fig. 5.2 (left) along with a comparison to the results published in [1] for the same $p_{\mathrm{T}}^{\mathrm{asso}}$ and $p_{\mathrm{T}}^{\mathrm{trig}}$ intervals (right). The analysis in the published letter deployed so-called *hybrid* track cuts and corrected with the pair-efficiency method discussed in sec. 4.4.1. Furthermore, the expectations from performing this subtraction method on MC reconstructed data (cf. sec. 4.6) are displayed in the projection plots as well, underlining that the observed double ridge structure was not anticipated from the MC-simulations. The double cosine fit function (eq. (4.9)) was found to be superior to a single cosine ($a_3 = 0$) fit yielding $\chi^2/NDF = 1.29$ compared to $\chi^2/NDF = 11.75$.
The ridge yield of the here presented method is compatible with the published results, however, the baseline for the yield extraction is found to be $\sim 5\%$ larger. This can be attributed to an error made in the published results[2] when applying the finite bin correction to the background normalization as described in sec. 4.2.2; the inverse of the correction α_{corr} was erroneously applied to the background rendering $B(\Delta\eta \approx 0, \Delta\varphi \approx 0)$ slightly larger than unity instead of smaller. Exact values of the bin width used in this correction are not available to the author but are expected to be $\sim 5\%$.
The same analysis was repeated with the $0.5\,\mathrm{GeV/c} < p_{\mathrm{T}}^{\mathrm{asso}} < 1\,\mathrm{GeV/c} < p_{\mathrm{T}}^{\mathrm{trig}} < 2\,\mathrm{GeV/c}$ interval and is summarized in fig. 5.3. The results from this interval are phenomenologically very similar to the first described interval. Again, a di-jet like structure was dominantly present for all four multiplicity classes while the most central one showed additional enhancement in the near-side long-range region. The subtraction between the highest and lowest multiplicity class is depicted in fig. 5.5(top left) exhibiting the double ridge. The $\Delta\eta$ projection in this plot also shows a small remainder of a jet-peak on the near side suggesting that the di-jet contributions are in fact not identical in the high and low multiplicity class.

5.2 With high p_{T} threshold

The following presents the results with the additional high p_{T} threshold in the event selection as described in sec. 4.1.2.
Fig. 5.4 (top) displays the evolution of $Y(\Delta\eta, \Delta\varphi)$ with increasing $p_{\mathrm{T}}^{\mathrm{thresh}}$ projected onto $\Delta\varphi$ for each event class. The peak region was excluded in the projections and the $p_{\mathrm{T}}^{\mathrm{asso}}$ and $p_{\mathrm{T}}^{\mathrm{trig}}$ intervals were set to $0.5 - 1\,\mathrm{GeV/c}$ and $1 - 2\,\mathrm{GeV/c}$. In order to highlight the relative changes in each event class the cases with a threshold $p_{\mathrm{T}}^{\mathrm{thresh}} > 0.0\,\mathrm{GeV/c}$ were divided by the results obtained when not requiring a high p_{T} threshold particle in the event selection criteria (fig. 5.4 (bottom)). All multiplicity classes exhibited an increase in the number of uncorrelated associated particles per trigger particle (seen as an increase of the baseline), peripheral events were found to have the largest relative gain in this regard. However, while the uncorrelated contributions were ordered by multiplicity in the projection shown on top, the order was not preserved in the bottom plots: the

[2] The decision was made to not update the public results since it was minor compared to the error of the extracted yields and v_3 while v_2 is not sensible to α_{corr}.

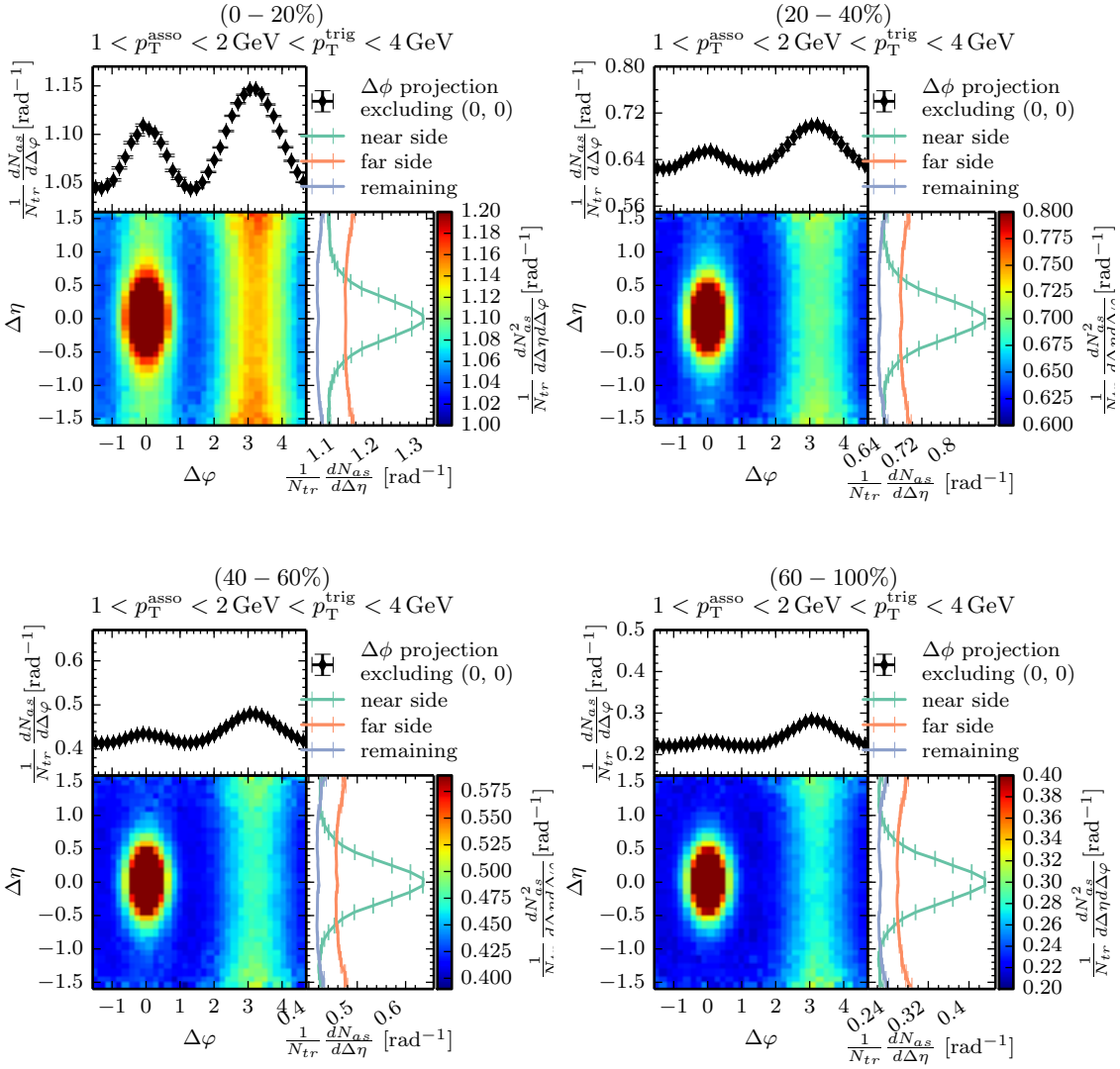

Figure 5.1: Total associated yield per trigger particle for all four multiplicity classes and the $p_{\mathrm{T}}^{\mathrm{asso}}$ ($p_{\mathrm{T}}^{\mathrm{trig}}$) interval of $1-2\,\mathrm{GeV/c}$ ($2-4\,\mathrm{GeV/c}$). The $\Delta\varphi$ projection excludes the jet peak area ($|\Delta\eta| < 0.8; \quad \pi/3 < \Delta\varphi < 2\pi/3$). The long range $\Delta\eta$ structure is decreasing in comparison to the away-side structure with decreasing multiplicity.

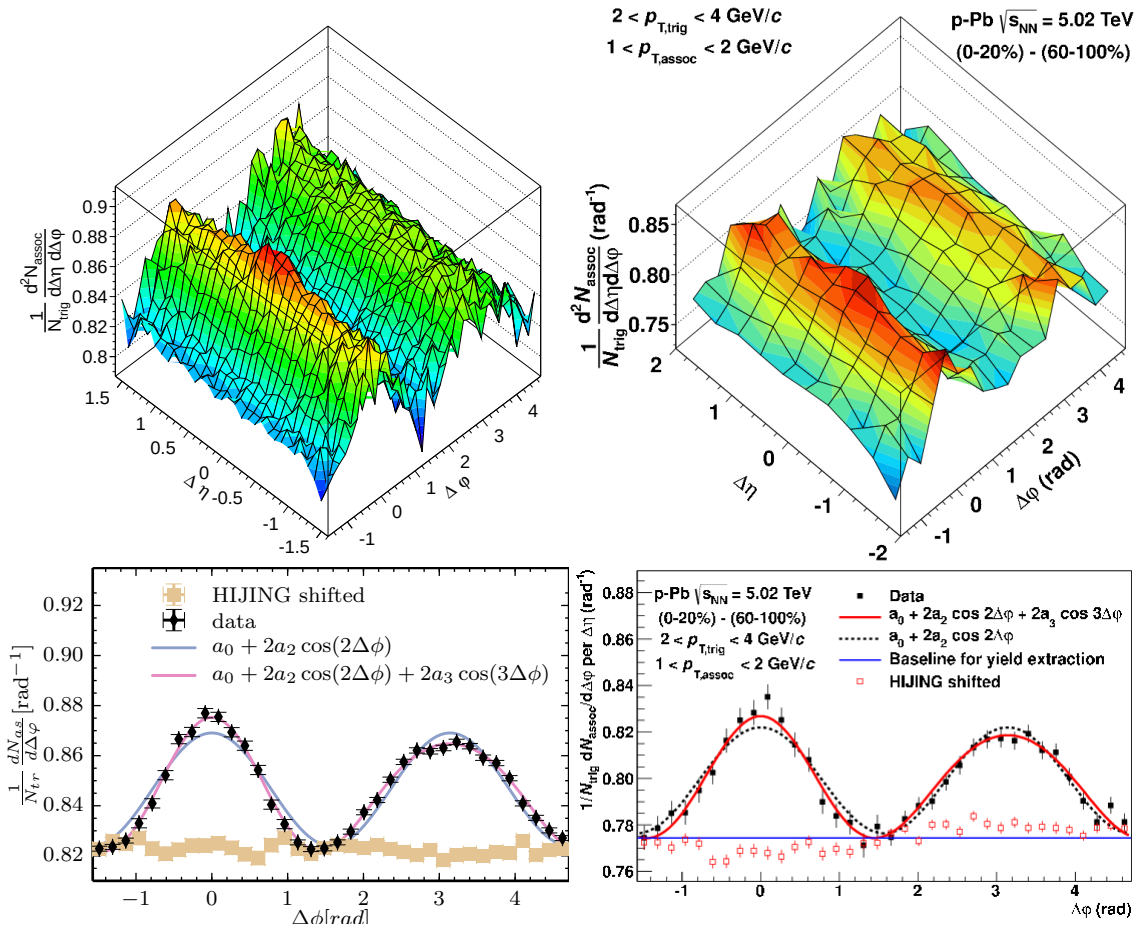

Figure 5.2: Subtraction of low multiplicity $Y(\Delta\eta, \Delta\varphi)$ from that computed for the high multiplicity class in the $p_{\mathrm{T}}^{\mathrm{asso}}$ ($p_{\mathrm{T}}^{\mathrm{trig}}$) interval of $1-2$ GeV/c ($2-4$ GeV/c). Left hand side: Results obtained with the methods described in chapter 4 for measured data. Right hand side: Results published in [1] for the same $p_{\mathrm{T}}^{\mathrm{asso}}$ and $p_{\mathrm{T}}^{\mathrm{trig}}$ intervals but corrected with the pair-efficiency method. The top right plot presents the $\Delta\eta$ projection for the near-side, away-side and remaining region analog to the $\Delta\eta$ projection in the left hand plot. Bottom right ($\Delta\varphi$ projection) and the $\Delta\varphi$ projection in the left hand plot exclude the jet peak region ($|\Delta\varphi| < \pi/3$, $0.8 < |\Delta\eta| < 1.6$). The method presented in sec. 4 reproduced the published results apart from an offset explained in the text.

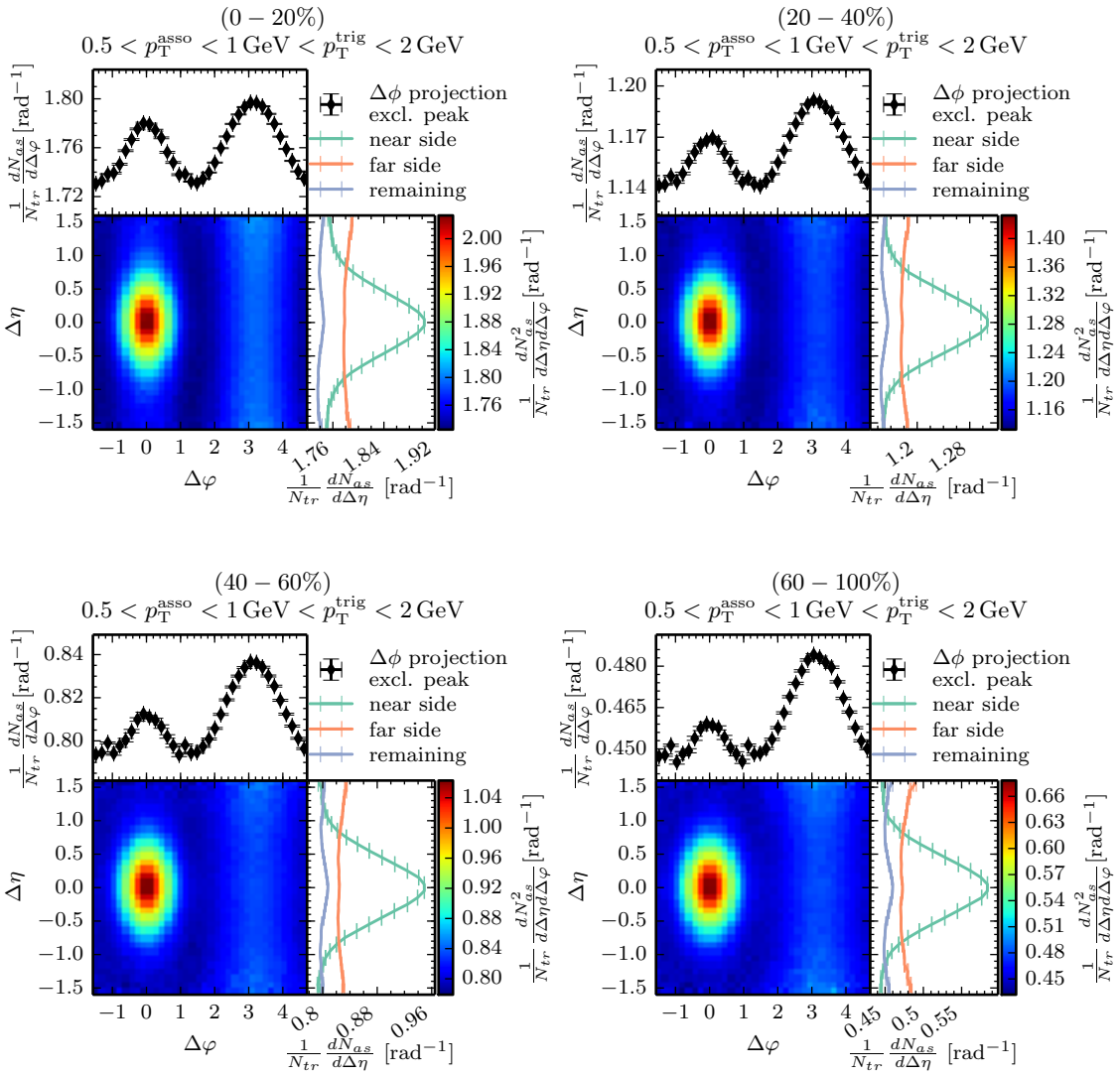

Figure 5.3: Equivalent to fig. 5.1 but for the interval of $0.5\,\mathrm{GeV/c} < p_{\mathrm{T}}^{\mathrm{asso}} < 1\,\mathrm{GeV/c} < p_{\mathrm{T}}^{\mathrm{trig}} < 2\,\mathrm{GeV/c}$. Again, a clear di-jet like structure is seen in all four multiplicity classes while only the highest one $(0-20\%)$ also exhibits an enhancement in the long-range regions of the near-side.

smallest increase of uncorrelated particles was observed for the $20 - 40\%$ event class. Regarding changes in the number of correlated particles all but the most central collisions displayed an increase of the away side yield. Furthermore, the most peripheral event class displayed a marginal increase on the near side yield (excluding the peak region).
Results for the subtraction method described in sec. 4.6 in combination with the high p_{T} threshold requirement are shown in fig. 5.5. The top left plot represents the no threshold case for comparison. As previously, the peak area was excluded for the $\Delta\varphi$ projection to be able to better investigate the long range near side ridge. The results obtained by applying the subtraction method to reconstructed data are shown in light brown in the $\Delta\varphi$ projection plots. It was observed that the measured away side yield approached the uncorrelated baseline for increasing values of $p_{\mathrm{T}}^{\mathrm{thresh}}$ while the long range contributions to the near-side ridge remained largely unchanged. The peak region of the near-side peak exhibited the emergence of a dip with increasing threshold as displayed in the $\Delta\eta$ projections.
The change of the away-side ridge yield (marked as gray area) can be attributed to the decrease in that area expected from the MC reconstructed data (cf. sec. 4.6). This observation was quantified by integrating the difference of the measured and MC reconstructed data over the interval $\pi/2 < \Delta\varphi < 3\pi/2$. The near-side ridge yield was further investigated by separating it into the jet peak area ($|\Delta\eta| < 0.8$) and the remaining long range contribution as depicted in fig. 5.6. These two areas were integrated over the interval of $-2\pi/2 < \Delta\varphi < \pi/2$. The results of these three yield extractions (away-side, near-side and peak region) are shown in fig. 5.7 along with the systematic uncertainties from the MC closure tests described in sec. 4.6. No $p_{\mathrm{T}}^{\mathrm{thresh}}$ dependence was found for any of these quantities outside of the margin of uncertainties.

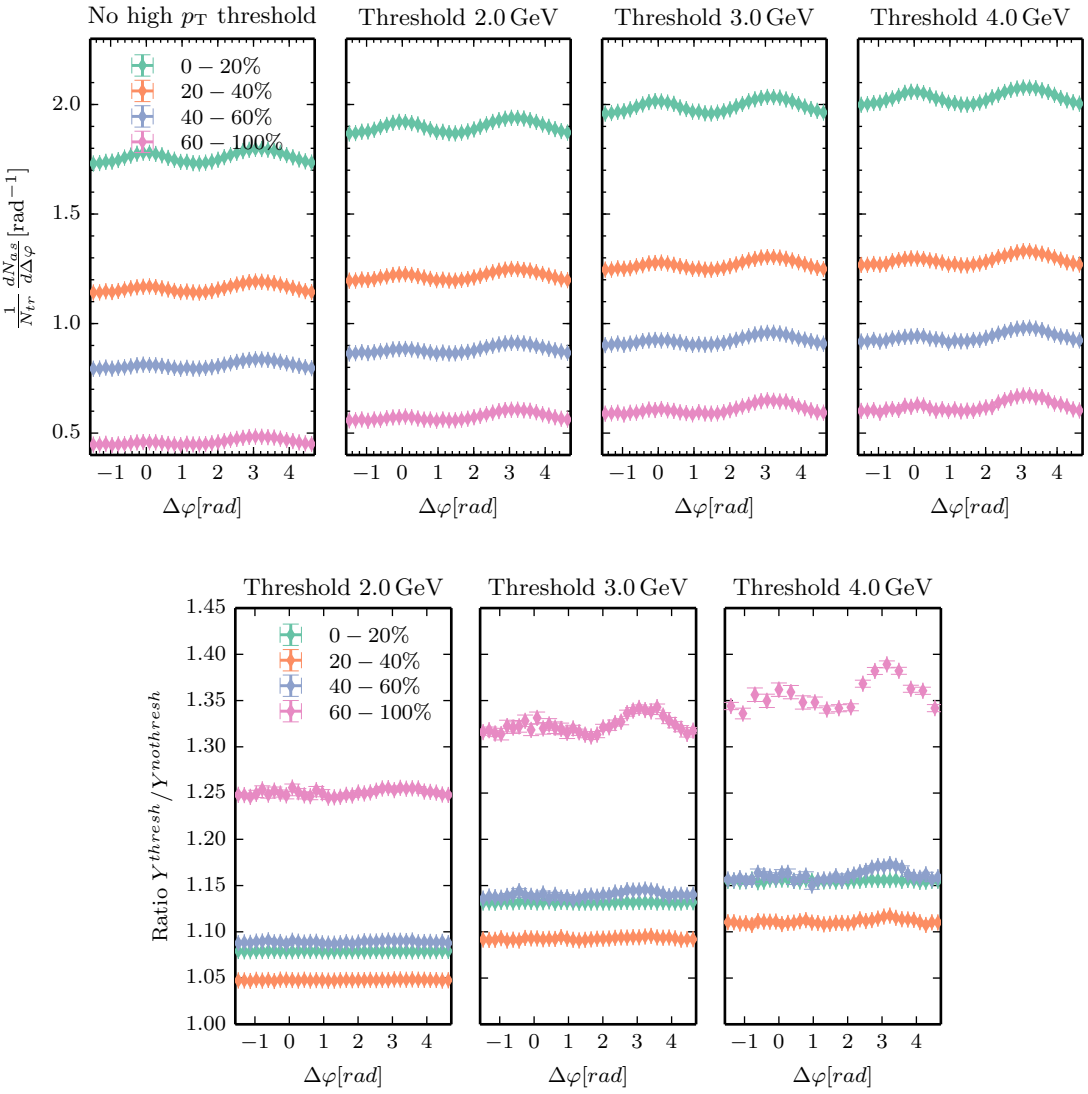

Figure 5.4: Effect of requiring a high p_T particle in the event selection. Top: Total associated yield per trigger particle as a projection onto $\Delta\varphi$ excluding the peak region for several values of p_T^{thresh} . Bottom: The cases with a enforced threshold were divided by the $p_T^{thresh} = 0.0$ GeV/c case to highlight relative changes in each event class. The threshold increased the baseline in all cases. The greatest change in baseline as well as shape was observed for the most peripheral event class. Only statistical uncertainties are shown.

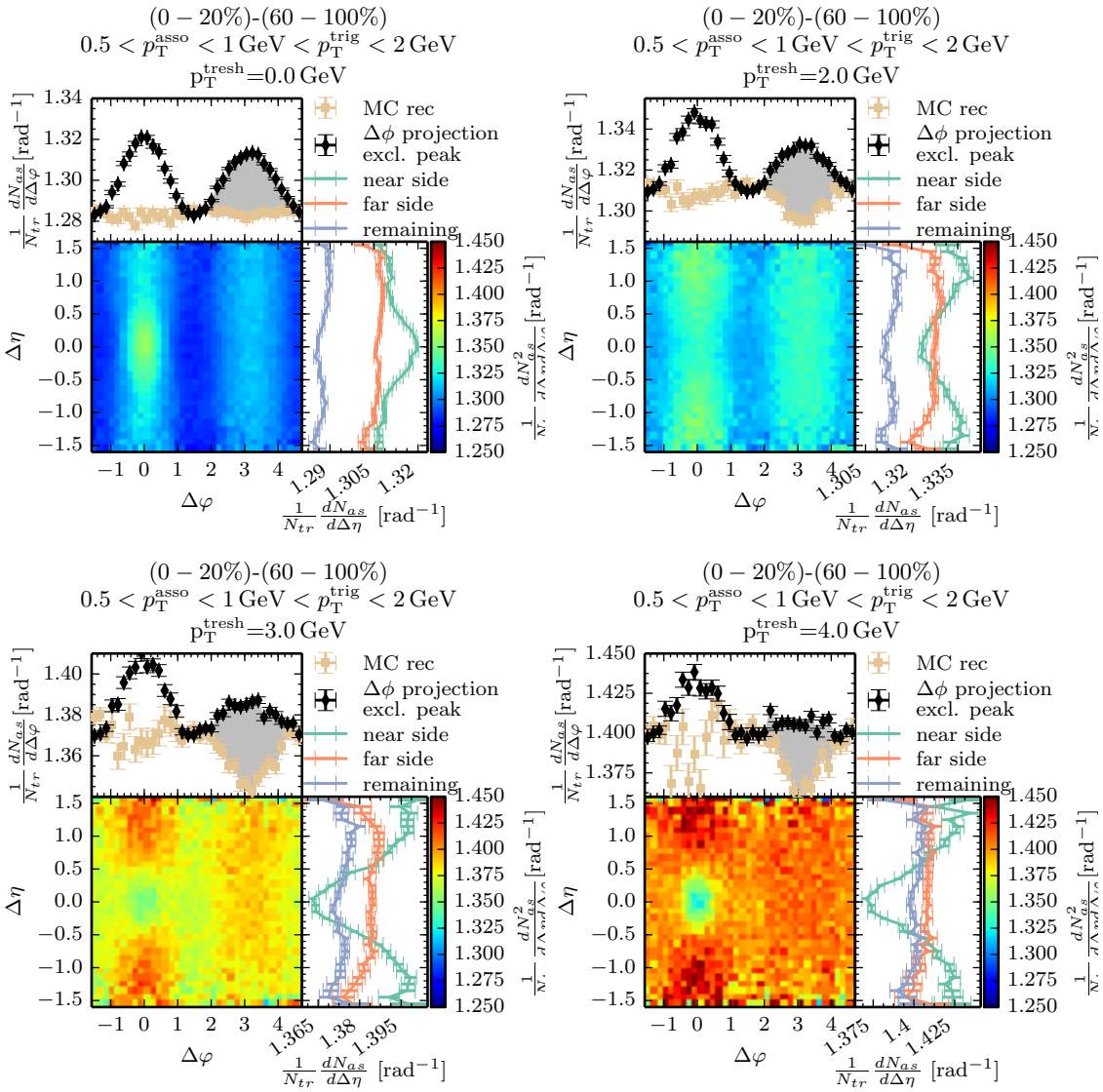

Figure 5.5: Results for subtracting $60-100\%$ from $(0-20\%)$. The results yielded by applying the analysis method onto MC reconstructed data is shown in the $\Delta\varphi$ projection in light brown. The area used for the extraction of the far side yield is marked gray. With increasing threshold a dip appears in the near side ridge while the away side ridge appears to vanish. The evolution of the away side yield is depicted in fig. 5.7

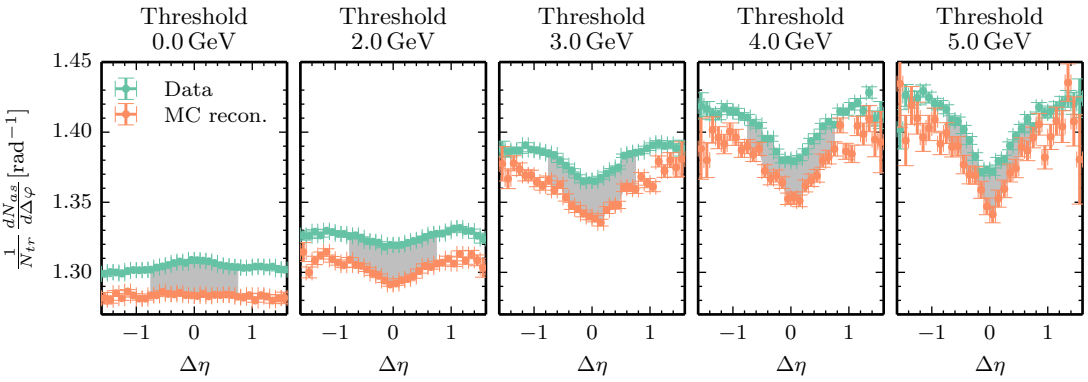

Figure 5.6: Near-side ridge as seen in the $\Delta\eta$ projection. The near side peak was extracted for the region marked grey, the long-range near-side yield was extracted from the region $0.8 < |\Delta\eta| < 1.8$ rad.

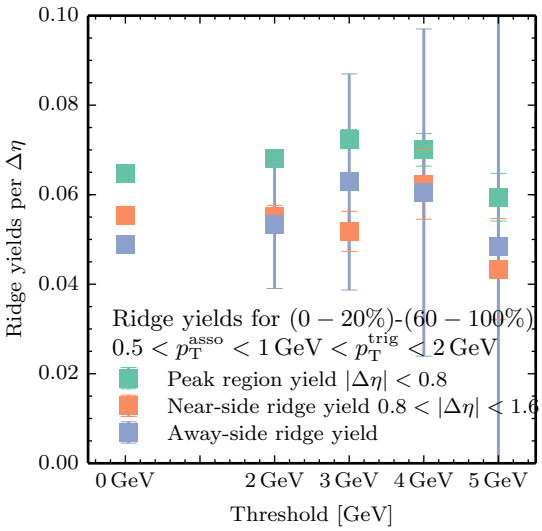

Figure 5.7: Evolution of the ridge yields with increasing threshold. The yields were extracted as described in sec. 4.6 and include the systematic uncertainty introduced by the non-closure at increasing thresholds.

Chapter 6

Discussion

The results shown in chap. 5 had two primary objectives. The first being the reproduction of the published results while applying the novel average-efficiency method (cf. sec. 4.4.2). This was achieved for all investigated intervals of $p_{\mathrm{T}}^{\mathrm{asso}}$ and $p_{\mathrm{T}}^{\mathrm{trig}}$ with respect to the ridge yields and base line of uncorrelated particles taking into account the fact that the published results were erroneously lowered by approximately 5% (cf. sec. 5.1). Thus, the implemented methods can be regarded as a well working foundation for the studies on the hardened event sample, but one further consideration has to be made before discussing the introduction of a threshold:
The motivation for the definition of the subtraction method was the assumption that the di-jet contributions were independent of the multiplicity class and would thus cancel each other, revealing only non-di-jet related differences. However, a remaining peak on the near side of the double ridge was observed after applying the subtraction in fig. 5.2 and fig. 5.5. This suggests that the jet contribution on the near-side are indeed not identical in the two multiplicity classes. Due to momentum conservation, this will also cause the recoils of the jets (the away side part of the di-jet structure) to be of different magnitude. However, this cannot be verified since the recoil coincides with the so far unexplained away side of the double-ridge. In the no-threshold cases, the mismatch between the two jet peaks, and thus their recoil was small in comparison to the total ridge size and could therefore be disregarded. However, the conclusion from this discussion is that the peak-region as well as the away side may include considerable di-jet contributions, if one of the centrality classes becomes biased towards jets as discussed below. However, it is important to note that the long-range near side is not affected by di-jets and thus represents an unbiased part of the double-ridge.

Fig. 5.4 (bottom) displays the dependence of $Y(\Delta\varphi)$ on $p_{\mathrm{T}}^{\mathrm{thresh}}$ for each multiplicity class relative to the no threshold case. The general baseline increase of all four classes can be attributed to the dependence of the number of charged particles N_{ch} to the $\langle p_{\mathrm{T}} \rangle$ (which is raised by the threshold) of the underlying event (cf. fig. 2.10) which is a well understood effect.

The enhancement of the away-side peak, on the other hand, is less clear. Events of the high multiplicity class $(0-20\%)$ may be expected to include several jets per event. The requirement of a high p_{T} particle will thus be met by a large subset of the initial event sample. On the other hand,

the same does not apply to the low multiplicity class ($60 - 100\%$): Events meeting the threshold criteria are likely to have only one di-jet which also includes its high p_{T} particle. Furthermore, only a small fraction of the original event sample will be available for further processing.
Hence, the low multiplicity event sample is expected to exhibit a strong bias towards di-jet events due to the threshold while the high multiplicity class is expected to be less enriched by hard events in comparison.

Together with the initial discussion about the possible mismatches of the di-jet contributions in the high and low multiplicity classes, this explains the dip on the near-side and negative ridge on the away-side seen when applying the subtraction method to MC-truth and MC-reconstructed data while requiring a threshold particle as shown in fig. 4.13.

Applying the subtraction method to experimental data, as shown in fig. 5.5, combines the above di-jet bias with the flow-like effect which is not included in the MC data. In this combination it appears as if the away-side vanishes completely at $4\,\mathrm{GeV/c}$ and above. It is intriguing that these two processes cancel each other so precisely and was, in fact, the very reason for the further investigation of the threshold effect. However, as of yet no convincing explanation for a connection between these two effects has been found.
At this point, it is clear that the threshold breaks the assumption that the di-jet contribution of the low multiplicity class cancels the one in the high multiplicity class. Hence, the long-range near-side is now the primary region for studying the evolution of the double ridge structure in hard events. However, a legitimate conclusion to this point is only possible if approximate MC closure exists for this region. Sec. 4.5.3 addressed this question but a further discussion about the long-range near-side will follow here. Fig. 4.10 shows that closure is achieved for the $0 - 20\%$ centrality class while a di-jet-like structure of non-closure is present for $60 - 100\%$. It should be noted that no direct connection between this structure and the above described bias towards di-jet events in low multiplicity collisions is found as of yet. The region of interest is, however, the long-range near side. The $\Delta\eta$ projection suggests that this region is in on the same level as the remaining baseline which in turn coincides with the one of the high multiplicity class. This is strongly suggestive that the here applied method did not systematically alter the long-range near-side.

Fig. 5.7 depicts the evolution of the ridge yields with increasing threshold and with systematic uncertainties from the subtraction of the MC-truth and MC-reconstructed results. This diminishes the significance of the away-side. The peak yield does not suffer such a large systematical error in this definition but has to be considered carefully due to the non-closure in this region. Neither of theses sources of uncertainty are present for the long-range near-side. No dependence of this observable on $p_{\mathrm{T}}^{\mathrm{thresh}}$ was found. This might indicate that the process causing the flow-like effect is indeed not sensitive to the hardening of the event sample which is the anticipated behavior of the CGC and hydrodynamic-expansion model but not of the CR for which deviations were expected (cf. sec. 2.3.3). This is, however, not sufficient to rule out CR yet. Detailed calculation for CR in pPb are still scarce, especially under the here investigated conditions, and may yield results in accordance to the here presented results when conducted.

Chapter 7

Summary

The unanticipated, previously reported [1, 13], flow-like effects in high multiplicity pPb collisions at $\sqrt{5.02}$ TeV gave rise to several possible theoretical explanations with mutually exclusive assumptions about the state of matter created immediately after the collision.

The thesis at hand deployed the technique of two-particle correlation functions on an event sample biased towards hard events to gather further insight into the structure of the studied collisions. In its course, a novel approach to the correction of detector efficiencies was also deployed.
The flow-like excess in the measurements compared to DPMJET generated data was found to be independent of the hardness of the event sample within the margin of statistical and systematical uncertainties. The prominent double-ridge which was formerly yielded by subtracting the low multiplicity two-particle correlation function from the high multiplicity one was, however, significantly altered. This can be contributed to the enhancement of the di-jet structure in low multiplicity.
The CGC and hydrodynamical model were expected to exhibit no dependence on the hardness of the underlying event while a dependency for CR was anticipated. The here presented findings are suggestive towards the former two but it is not yet possible to discard CR as the origin of the flow-like behavior.
Further studies on the origin of the MC non-closure for hard event samples have to be conducted in order to significantly decrease the systematic uncertainty making the findings more conclusive. Furthermore, the deployment of a track clustering algorithm for the selection of hard events might improve the quality of the hardened event sample enhancing on the flow-like behavior. Furthermore, this thesis focused on the hardened event sample but similar studies on the softened sample would be the most important complement to these studies.
Even when not conclusively ruling out, or confirming one of the three proposed and discussed models explaining the double-ridge structure, this thesis still delivers valuable further insight into the properties of pPb collisions, which is much needed in the further understanding of the observed flow-like effects.

Appendix A

Appendix

A.1 Further discussion about total assocaited yield per trigger particle

A simple subtraction of B from S is not sufficient since the genuine correlations are distorted by the same principles discussed in sec. 4.2.2. A division, however, can only be justified under two assumptions: The division would yield a distribution with a flat baseline of uncorrelated events correcting for particle pairs with one constituent outside of the detector acceptance limits $\pm\eta_m$. However, this correction is only valid if the particle densities $dN/d\eta$ of the correlated and uncorrelated particles extend beyond $\pm\eta_m$ without exceptional features. The latter is justified by studies of the pseudo rapidity presented in [7]. Secondly, a division of S and B assumes that the particle densities $dN/d\eta$ of the correlated and uncorrelated particles are similar. Otherwise, the contribution from the correlated particles would be distorted differently than that of the uncorrelated ones. While these assumptions are usually met in symmetric collisions they seem to be also suitable for many p-Pb analyzes as well [9, 1, 13].

A.2 Biases in two-particle correlation functions

A collision can only contribute to $Y(\Delta\eta, \Delta\varphi)$ if it has at least one reconstructed trigger (cf. sec. 4.2.1). Thus, an event is lost to the analysis if none of its triggers were reconstructed; a scenario whose probability to occur is given by

$$P = 1 - \prod_{i}^{N}(1 - \epsilon_i) \tag{A.1}$$

where N is the total number of produced trigger particles and ϵ_i is the detector efficiency for each particle i given as $\epsilon(\eta_i, \varphi_i, p_{\mathrm{T},i}, z_{\mathrm{vtx},i})$. Figure A.1 (left) shows how the distribution of the number of triggers varies between MC-truth and MC-reconstructed data. The right hand plot displays that this effect also depends on the requirement of a high p_{T} threshold particle: The mean number of triggers of events with such a particle is increased in comparison to the original event sample.

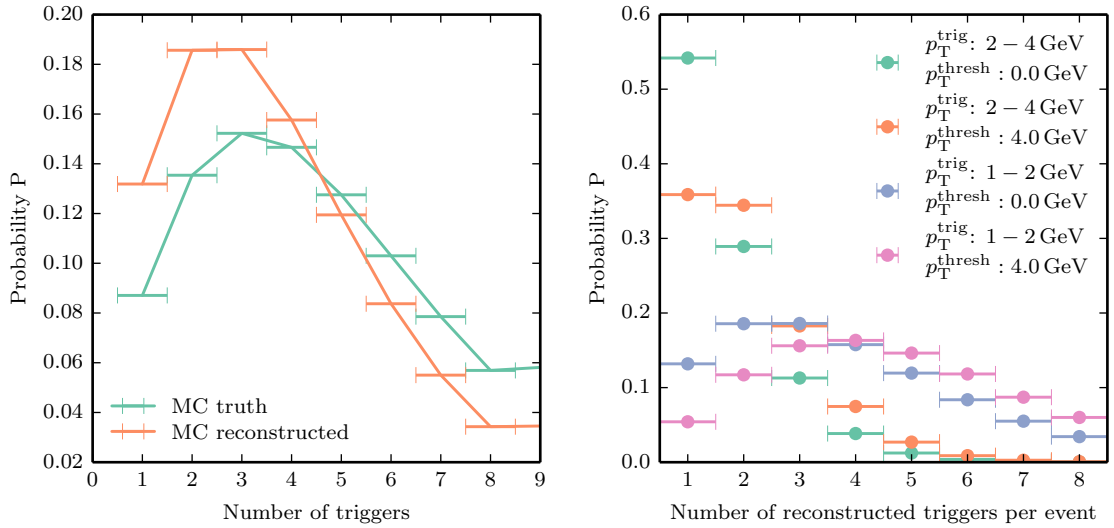

Figure A.1: Investigation into trigger multiplicity effects. Left: Normalized distributions of the number of triggers within an event for MC-truth and MC-reconstructed data in the p_T^{trig} interval is $1 - 2$ GeV/c. Right: Distributions for reconstructed data in different p_T^{trig} intervals with and without a high p_T threshold.

It is well possible that an events particle density distribution, which manifests itself in the $B(\Delta\eta, \Delta\varphi)$ (eq. (4.4)) and hence $S(\Delta\eta, \Delta\varphi)$, depends on the number of triggers produced in a collision. Eq. (A.1) states that the chance of an event contributing to the analysis also depends on its number of trigger. Thus, a bias towards events with a higher number of triggers is introduces.

A.3 Alternative efficiency correction by total associated yield ratios

The following method was developed during this thesis to correct for the observed non closure when requiring a high p_T particle in the event selection (cf. sec. 4.5.3) after not succeeding to fix the analysis method in this regard. This method corrects $Y(\Delta\eta, \Delta\varphi)$ with the observed non closure. This approach introduces a strong model dependence which would require further investigation. This method was thus discarded in favor of the one discussed in sec. 4.4.2. It was included here since it is still a valid method when investigating systematic uncertainty.
The starting point of this method is the interpretation of the uncorrected ratio of Y^{recon}/Y^{truth} as an efficiency correction $\epsilon(\Delta\eta, \Delta\varphi)$ itself. Corrected results can then be obtained by dividing Y by $\epsilon(\Delta\eta, \Delta\varphi)$. However, several dependencies have to be taken into account regarding this method:

- As shown in fig. 4.10, $\epsilon(\Delta\eta, \Delta\varphi)$ is dependent on the multiplicity class.
- Fig. 4.7 and 4.8 exhibit the dependence on the associated and trigger intervals.
- Fig. 4.8 and 4.11 (left hand plot) show the scale dependence of $\epsilon(\Delta\eta, \Delta\varphi)$ on the chosen cut.

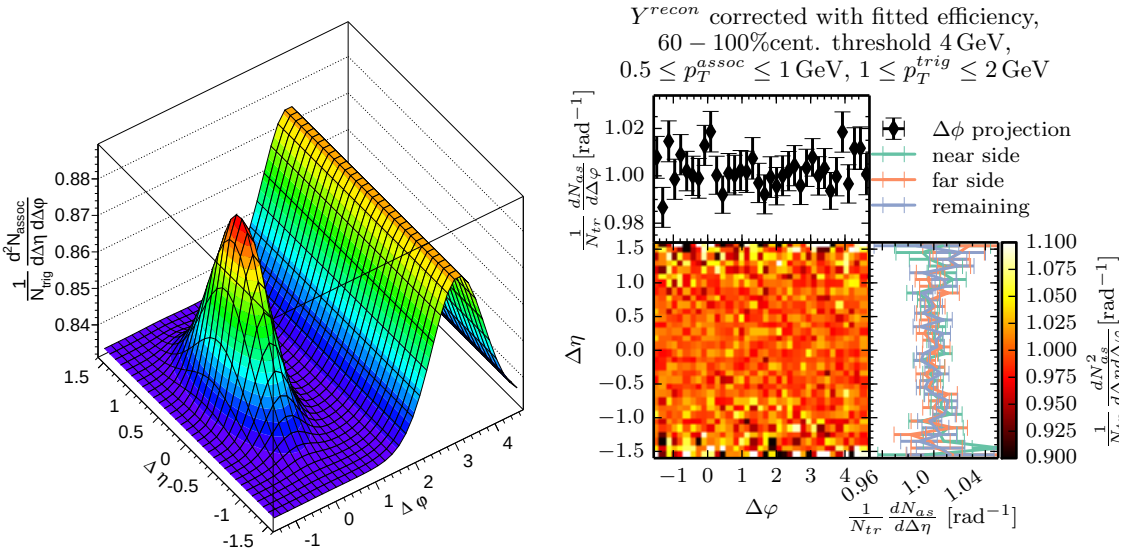

Figure A.2: Correction for non closure effects shown in fig. 4.10 (bottom right). Left: Non closure fitted with a two dimensional Gaussian on the near-side and a one dimensional one on the away-side. Right: Y^{recon} corrected with the fitted function and divided by Y^{truth} .

Thus, individual $\epsilon(\Delta\eta, \Delta\varphi)$ have to be computed for each of these parameters. In comparison, a single track efficiency only has to be computed once for each cut and can than be reused for all multiplicity classes, associated and trigger intervals. Hence the former method poses a much smaller degree of re-usability and generality while significantly increasing the computation requirements.
Another issue with $\epsilon(\Delta\eta, \Delta\varphi)$ lies in the fact that it introduces unnecessary[1] statistical uncertainties from MC data into the measurement. This shortcoming was addressed by fitting $\epsilon(\Delta\eta, \Delta\varphi)$ with a two dimensional Gaussian on the near side and an one dimensional Gaussian on the far side.
The application of this method is demonstrated for the case shown in fig. 4.10 (bottom right). The ratio of $Y^{\text{recon}}/Y^{\text{truth}}$ was fitted with the above described function. In this case the best fit yielded $\chi^2/NDF = 0.60$ and is displayed in fig. A.2 (left hand side). Dividing the initial ratio by that function yielded the results shown on the right hand side. The structure in $\Delta\eta$ and $\Delta\varphi$ observed in the projections of the initial ratio was successfully canceled within uncertainties in most bins. This, along with the afore stated normalized χ^2 value, is an indicator that the chosen fit function was suitable. Albeit, it has to be noted that the statistical uncertainties at large $\Delta\eta$ might disguise a distortion along that axis.

[1] Unnecessary in a sense that it could be overcome by having more generated MC events.

Acronyms

AA nucleus-nucleus
ALICE A Large Ion Collider Experiment
ATLAS A Toroidal LHC Apparatus

CERN Conseil Européen pour la Recherche Nucléaire
CGC Color Glass Condensate
CMS Compact Muon Solenoid
CR Color Reconnection

DCA Distance of Closest Approach

ITS Inner Tracking System

LEP Large Electron–Positron Collider
LHC Large Hadron Collider
LHCb Large Hadron Collider beauty

MC Monte Carlo
MWPC Multi Wire Proportionality Chamber

pA proton-lead
Pb lead
PbPb lead-lead
PID Particle Identification
pp proton-proton
pPb proton-nucleus

QCD Quantum Chromodynamics
QED Quantum Electrodynamics
QGP Quark Gluon Plasma

SDD Silicon Drift Detectors
SM Standard Model
SPD Silicon Pixel Detectors
SSD Silicon mico-Strip Detectors

TOF time-of-flight
TPC Time Projection Chamber

Bibliography

[1] Betty Abelev et al. “Long-range angular correlations on the near and away side in p-Pb collisions at sqrt(sNN) = 5.02 TeV”. In: (2012).

[2] Betty Abelev et al. “Transverse Momentum Distribution and Nuclear Modification Factor of Charged Particles in p-Pb Collisions at $\sqrt{s_{NN}} = 5.02$ TeV”. In: *Phys.Rev.Lett.* 110 (2013), p. 082302. DOI: 10.1103/PhysRevLett.110.082302.

[3] D. Acosta et al. “Soft and hard interactions in $p\overline{p}$ collisions at $\sqrt{s} = 1800$ and 630 GeV”. In: *Phys. Rev. D* 65 (7 2002), p. 072005. DOI: 10.1103/PhysRevD.65.072005.

[4] Andrew Marshall Adare. *Harmonic decomposition of two particle angular correlations in Pb-Pb collisions at 2.76 TeV*. https://aliceinfo.cern.ch/Figure/node/2229. [Online; accessed 8-March-2014]. 2012.

[5] Andrew Marshall Adare. *Harmonic decomposition of two particle angular correlations in Pb-Pb collisions at 2.76 TeV*. https://aliceinfo.cern.ch/Figure/node/2231. [Online; accessed 8-March-2014]. 2012.

[6] Ahmed Ali, Christian Hambrock, and M. Jamil Aslam. “Tetraquark Interpretation of the BELLE Data on the Anomalous Resonance”. In: *Phys. Rev. Lett.* 104 (16 2010), p. 162001. DOI: 10.1103/PhysRevLett.104.162001.

[7] ALICE Collaboration. “Pseudorapidity density of charged particles in p-Pb collisions at sqrt(sNN) = 5.02 TeV”. In: *ArXiv e-prints* (Oct. 2012).

[8] Anton Andronic. *Average transverse momentum as a function of charged particle multiplicity data and models +EPOS for pp*. https://aliceinfo.cern.ch/Figure/node/4847. [Online; accessed 8-March-2014]. 2013.

[9] ATLAS Collaboration. “Observation of Associated Near-side and Away-side Long-range Correlations in sqrt(s_NN)=5.02 TeV Proton-lead Collisions with the ATLAS Detector”. In: *ArXiv e-prints* (Dec. 2012).

[10] Christian Bourjau. *Source code for the study of two particle long-range angular correlations in soft and hard pPb collisions at the LHC*. https://github.com/chrisboo/2_particle_correlations. [Online; accessed 12-March-2014]. 2014.

[11] Piotr Bozek and Iwona Wyskiel. “Directed flow in ultrarelativistic heavy-ion collisions”. In: *Phys.Rev.* C81 (2010), p. 054902. DOI: 10.1103/PhysRevC.81.054902.

[12] Serguei Chatrchyan et al. “Indications of suppression of excited Υ states in PbPb collisions at $\sqrt{S_{NN}}$ = 2.76 TeV”. In: *Phys.Rev.Lett.* 107 (2011), p. 052302. DOI: 10.1103/PhysRevLett.107.052302.

[13] S. CMS Collaboration Chatrchyan et al. “Observation of long-range, near-side angular correlations in pPb collisions at the LHC”. In: *Physics Letters B* 718 (Jan. 2013), pp. 795–814. DOI: 10.1016/j.physletb.2012.11.025.

[14] The ALICE Collaboration et al. “The ALICE experiment at the CERN LHC”. In: *Journal of Instrumentation* 3.08 (2008). Very detailed description of the Alice detector, S08002.

[15] G. Cotugno et al. “Charmed Baryonium”. In: *Phys.Rev.Lett.* 104 (2010), p. 132005. DOI: 10.1103/PhysRevLett.104.132005.

[16] Cush. *Standard Model of Elementary Particles*. https://en.wikipedia.org/wiki/File:Standard_Model_of_Elementary_Particles.svg. [Online; accessed 8-March-2014]. 2014.

[17] David d’Enterria. “Quark-Gluon Matter”. In: *J.Phys.* G34 (2007). general overview QGP, S53–S82. DOI: 10.1088/0954-3899/34/7/S04.

[18] K. Dusling and R. Venugopalan. “Explanation of systematics of CMS p+Pb high multiplicity di-hadron data at $\sqrt{s}_{\rm NN} = 5.02$ TeV”. In: *ArXiv e-prints* (Nov. 2012).

[19] Kevin Dusling and Raju Venugopalan. “Comparison of the color glass condensate to dihadron correlations in proton-proton and proton-nucleus collisions”. In: *Phys.Rev.* D87.9 (2013), p. 094034. DOI: 10.1103/PhysRevD.87.094034.

[20] F. Englert and R. Brout. “Broken Symmetry and the Mass of Gauge Vector Mesons”. In: *Phys. Rev. Lett.* 13 (9 1964), pp. 321–323. DOI: 10.1103/PhysRevLett.13.321.

[21] F. Gelis. “Color Glass Condensate and Glasma”. In: *Int.J.Mod.Phys.* A28 (2013), p. 1330001. DOI: 10.1142/S0217751X13300019.

[22] Jan Fiete Grosse-Oetringhaus. *Associated yield per trigger particle, 0-20%*. https://aliceinfo.cern.ch/Figure/node/3991. [Online; accessed 8-March-2014]. 2012.

[23] Jan Fiete Grosse-Oetringhaus. *Associated yield per trigger particle, 0-20% minus 60-100%*. https://aliceinfo.cern.ch/Figure/node/3994. [Online; accessed 8-March-2014]. 2012.

[24] Jan Fiete Grosse-Oetringhaus. *Associated yield per trigger particle, 60-100%*. https://aliceinfo.cern.ch/Figure/node/3990. [Online; accessed 8-March-2014]. 2012.

[25] Gosta Gustafson. “Multiple Interactions, Saturation, and Final States in pp Collisions and DIS”. In: *Acta Phys.Polon.* B40 (2009), pp. 1981–1996.

[26] Peter W. Higgs. “Broken Symmetries and the Masses of Gauge Bosons”. In: *Phys. Rev. Lett.* 13 (16 1964), pp. 508–509. DOI: 10.1103/PhysRevLett.13.508.

[27] D. Manglunki. May 2001.

[28] S. Manly et al. “System size, energy and pseudorapidity dependence of directed and elliptic flow at RHIC”. In: *Nucl.Phys.* A774 (2006), pp. 523–526. DOI: 10.1016/j.nuclphysa.2006.06.079.

[29] Andreas Morsch. “p-Pb Results from ALICE with an Emphasis on Centrality Determination”. In: (2013).

[30] B. Odom et al. “New Measurement of the Electron Magnetic Moment Using a One-Electron Quantum Cyclotron”. In: *Phys. Rev. Lett.* 97 (3 2006), p. 030801. DOI: 10.1103/PhysRevLett.97.030801.

[31] Antonio Ortiz et al. “Color reconnection and flow-like patterns in pp collisions”. In: *Phys.Rev.Lett.* 111 (2013), p. 042001. DOI: 10.1103/PhysRevLett.111.042001.

[32] Stefan Roesler, Ralph Engel, and Johannes Ranft. “The Monte Carlo event generator DPMJET-III”. In: (2000), pp. 1033–1038.

[33] Stefan Scherer. *Dynamics of Coloured Quarks: The Quark Gluon Plasma in the Computer*. 2004.

[34] T. Schuster and A. Morsch. “Mixed-event corrections for two-particle angular correlations”. In: ALICE Physics Club. 2013.

[35] Jochen Thaeder. *3D ALICE Schematic*. https://aliceinfo.cern.ch/Figure/node/3400. [Online; accessed 2-February-2014]. 2012.

[36] Alberica Toia. *V0A centrality in pPb + Glauber-NBD fit*. https://aliceinfo.cern.ch/Figure/node/4492. [Online; accessed 8-March-2014]. 2013.

[37] ulia Velkovska, Vanderbilt University, and Gabor Veres. “CMS studies the quark–gluon plasma”. In: *Cern Courier: September 2012* (2012).

[38] Vytautas Vislavicius. “Azimuthal Angular Description of Jet Quenching at High pT”. MA thesis. 2013.

[39] S. Voloshin and Y. Zhang. “Flow Study in Relativistic Nuclear Collisions by Fourier Expansion of Azimuthal Particle Distributions”. In: *ArXiv High Energy Physics - Phenomenology e-prints* (July 1994).

[40] F. Wojciech. *Phenomenology of Ultra-relativistic Heavy-ion Collisions*. World Scientific, 2010. ISBN: 9789814280686.

[41] Lingshan Xu, Chin-Hao Chen, and Fuqiang Wang. “Dividing by mixed-events for acceptance correction is wrong”. In: (Apr. 2013).